Self-Shading Corrections for MOBY Upwelling Radiance Measurements

Final Technical Report NOAA Grant NA04NES440007:

"Reduced Uncertainties in Measurements of Water-Leaving Radiance, and Other Optical Properties, Using Radiative Transfer Models and Empirical Data Analysis":

PI: James L. Mueller
Institution: SDSU Research Foundation

Introduction

The primary goal of the research under this grant is to determine the effect of instrument self-shading in upwelling radiance measurements by a downward viewing detector that is located in water beneath an instrument housing having an arbitrarily shaped horizontal cross-section. Of special interest in this context are self-shading corrections for the upwelling radiance measurements on the NOAA Marine Optical BuoY (MOBY), which is operated in clear, Case I water off the island of Lanai, Hawaii to provide measurements for vicarious calibration of satellite ocean color sensors (Clark et al. 2003).

The methods and computer software developed in this project, used in combination with the commercially licensed Hydrolight forward radiative transfer model (Mobley 1994; Mobley and Sundman 2000a, 2000b), apply to an instrument with a horizontal cross section of arbitrary shape and a detector aperture located at some depth Z below the water surface. The method of solution takes into account bidirectional effects associated with varying solar zenith and azimuth angles, sky conditions, and sea surface roughness associated with wind-driven capillary waves, as well as the bidirectional effects associated with specific inherent optical properties (IOP).

This Final Technical Report amounts to an extended abstract of a much more detailed Technical Manual, entitled "Instrument Self-Shading Correction Algorithms for Upwelling Radiance Sensors: Reciprocity Solutions for Arbitrary Instrument Shapes using Adjoint Monte Carlo and Forward Radiative Transfer Models," henceforth referred to here as ISSAMC TM. The PI (J. Mueller) compiled the ISSAMC TM, over the several years duration of this project, to provide a reference guide to, and record of, the lengthy and relatively complicated process of adapting the methods, numerical representations and computer codes used to derive the MOBY self-shading results presented here. A copy the ISSAMC TM, together with several gigabytes of MOBY self-shading arrays, will be separately delivered to NOAA NESDIS on a DVD-R.

Equations, Tables and Figures appearing in the present document retain the number identification from their occurrence in chapters of the ISSAMC Tech Manual.

The method used in this study builds on the backward Monte Carlo methods of Gordon (1985) and Gordon and Ding (1992; henceforth GD), who solved the instrument self-shading problem for a nadir-viewing upwelling radiance sensor centered under a horizontal, flat circular disk located just beneath the sea surface [denoted $z = 0_w$ here, following Mobley (1994), and elsewhere as $z = 0^-$]. GD showed that the self-shading effect is primarily dependent on the ratio of the instrument radius r to absorption scale length a^{-1}, and provided relatively simple empirical models dependent on ra, solar zenith angle, and the ratio of direct solar irradiance to sky irradiance $\frac{E_{sun}}{E_{sun}}$.

There are many important exceptions to this concentric viewing geometry, and we emphasize three:

1. The case of primary interest is a nadir-viewing radiance sensor aperture located under, and within a few cm of one end of, a rectangular boom of length 2 to 3 m and width ~5 cm. The boom is mounted to a spar buoy at the end away from the aperture (Fig. 6.2). This configuration is used on MOBY to place the radiometric sensors away from shadows and reflections from the flotation buoy (Clark *et al*. 2003). As shown below, the effects of shadows cast by the boom and spar cross section vary strongly with the azimuth angle between the boom direction and the sun.
2. A second case applies to the Marine Optical Sensor (MOS), which is deployed from ships for upwelling radiance measurements in MOBY development and validation experiments. The MOS, and radiance sensors on some other moored and free-drifting buoys (Kuwahara *et al.* 2003), have a nadir-viewing radiance aperture located away from the center of a cylindrical instrument housing (diameters ranging from 10 to 50 cm), or buoy hull (diameters between 0.5 and 3 m). In many such cases, the motivation is to orient the platform so that the sensor aperture offset is generally in the direction of the solar azimuth, in the hope of thus reducing the influence of self-shading. Self-shading corrections for this case require that the sensor-offset azimuth is known at the time of the measurement.
3. Another configuration that appears on some moored and free-drifting buoy consists of radiance sensor viewing upwelling radiance at a nadir-angle away from zero, again located under, and towards one edge of, a buoy hull having a circular horizontal cross-section (Kuwhara *et al.* 2003). This viewing geometry may indeed result in less shadowing than nadir viewing geometry, but it also introduces asymmetric bi-directionality, associated with the ocean IOP, that has not yet been quantitatively determined and considered. Although the extension of the present methods and software to the off-nadir viewing case is straightforward, each Adjoint Monte Carlo solution would require tracking an order of magnitude more photon packet trajectories than are required for the nadir viewing case discussed in this report.

The scope of the present report is limited to the first of the above three cases, *i.e.* to self-shading by the MOBY spar buoy and boom cross sections as a function of solar zenith and azimuth angles for a range of ocean IOP typical of the MOBY site. The methods and software developed for that purpose can easily be applied directly to any combination of Cases 1 and 2, given the appropriate geometric and radiometric parameters and IOP profiles, but we have not done so. The formalism of the methods presented in the ISSAMC TM apply as well to Case 3, and it would be straightforward to modify the computer codes to that end, but the computations would be formidable (several hours per vertically homogeneous IOP state for the 80-wavelength solutions presented here) and this problem

is beyond the scope of the present project and report. The computer codes developed to support this project will also compute solutions for vertically varying profiles of IOP, which must be specified externally. At the outset of this project, we anticipating running such cases, but available time and resources under this grant were not adequate to include them.

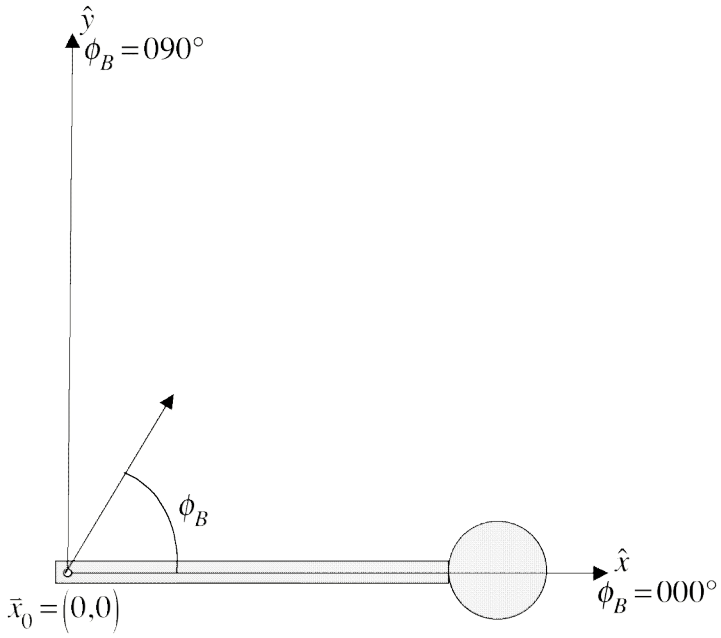

Fig. 6.2: Schematic cross section of the MOBY Spar buoy (the shaded circle) and a radiometric sensor standoff boom, viewed from below to be consistent with the Z-axis being positive in the downward direction. The nadir-viewing upwelling radiance sensor aperture is located at the origin, an azimuth is measured counter-clockwise in the horizontal plane containing the sensor. Note that when these coordinates are viewed from above (i.e. from behind the paper), the solar azimuth relative to the Boom/Spar direction (from the aperture) is calculated as $\phi_0 = \phi_{\text{True}}^{\text{Sun}} - \phi_{\text{True}}^{\text{Boom/Spar}}$, where the subscript "True" indicates the corrected compass directions, relative to True-North, of the sun and boom/spar axis, respectively.

Forward and Adjoint Radiative Transfer and Reciprocity

The relationship between forward and adjoint (backward) radiative transfer processes is illustrated in Fig. 1.1 (following Mobley 1994). Here we index radiometric quantities in the forward problem with the subscript "2", and those associated with the adjoint problem with the subscript "1".

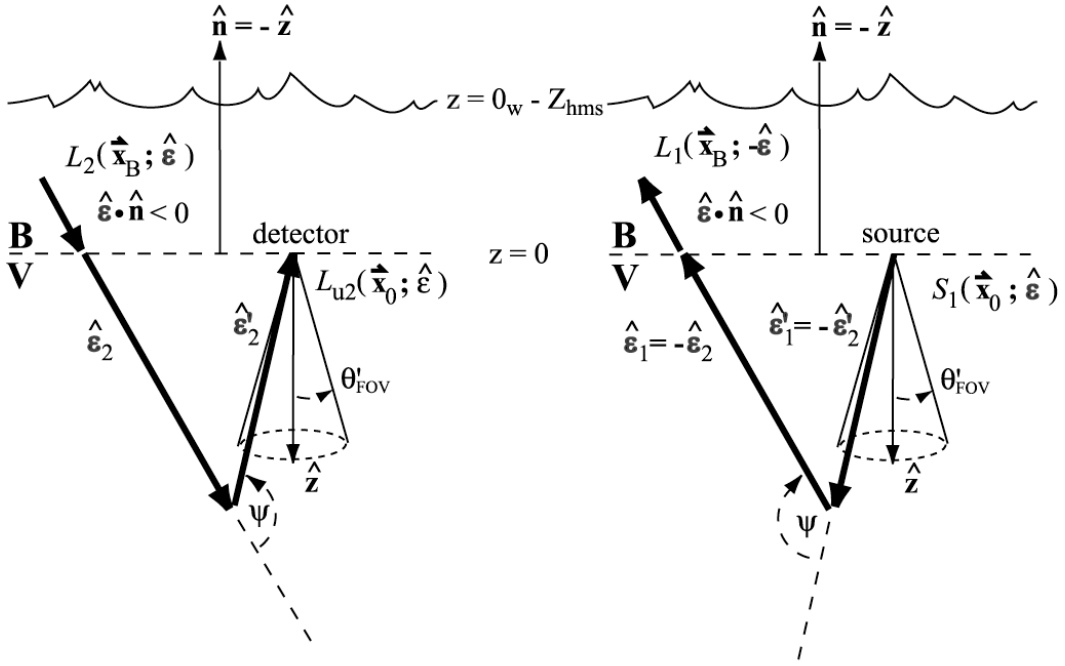

a. Case 2: Forward Problem **b**. Case 1: Adjoint Problem

Figure 1.1. Schematic illustration of the forward (panel a) and adjoint (panel b) problem used as a basis for the backward Monte Carlo solution. This figure is modeled after Fig. 6.2 in Mobley (1994). In the present case, however, the horizontal monitoring surface (hms) forming the boundary **B** is the *xy*-plane located at depth $z_{\text{sfc}} = 0_{\text{w}} - Z_{\text{hms}}$, and the volume **V** is the water column below that depth. The source/detector location $\vec{\mathbf{x}}_{\text{o}}$ lies in the boundary **B**. HYDROLIGHT, or another convenient radiative transfer model, may be used to determine the forward problem radiance distribution $L_2\left(\vec{x}_{\text{B}};\hat{\varepsilon}\right)$ for any given solar elevation and zenith angles, sky conditions, and wind-driven, wave-roughened sea surface. The in-water choice of hms decouples the adjoint Monte Carlo solution from the sea surface boundary conditions, and yields a solution dependent only on the ocean's IOP and the upwelled radiance detector's solid angle field-of-view $\left|\vec{\Omega}_{\text{FOV}}\right| = 2\pi\theta'_{\text{FOV}}$ and viewing direction $\hat{\varepsilon}_{\text{FOV}}$. For the present we will consider only nadir-viewing geometry, i.e. $\hat{\varepsilon}_{\text{FOV}} \bullet \hat{\text{z}} = 1$ and $\cos\theta'_{\text{FOV}} \le \hat{\varepsilon}_1 \bullet \hat{\text{z}} \le 1$, which yields an azimuthally symmetric adjoint solution for any radial vector in **B** measured from $\vec{\mathbf{x}}_{\text{o}}$. Symmetry in this case simply means that the adjoint upwelled directional distribution of radiance in **B** at a given radial distance r_{B} is azimuthally fixed relative to $\vec{r}_{\text{B}}$ and is independent of direction from $\vec{\mathbf{x}}_{\text{o}}$. This symmetry does not exist for a non-nadir viewing/source direction $\hat{\varepsilon}_{\text{FOV}} \bullet \hat{\text{z}} < 1$, and therefore, the adjoint Monte Carlo solution for that problem is more computationally intensive.

In both the forward and backward cases:

a) Surface boundary conditions, *i.e.* incident radiance distributions, and the wind-driven sea surface slope distribution are horizontally constant for a given reciprocity solution.

b) IOP (absorption coefficient, scattering coefficient, and scattering phase function) are allowed to vary vertically, but are horizontally homogeneous.
c) Upwelling radiance is measured with a nadir-viewing sensor located on a horizontal monitoring surface (hms) Z_{hms} m below the sea surface (denoted **B** in Fig. 1.1). Note that in these coordinates, *z* is positive downward, the sea surface is at depth $z_{\text{sfc}} = 0_{\text{w}} - Z_{\text{hms}}$ and the hms **B** is at depth $z = 0$. The reader is referred to the ISSAMC TM (Chapters 1 and 2) for notational definitions and detailed descriptions of geometric relationships representing photon paths and photon-matter interactions in this coordinate system.

The reciprocity interaction principle states that the probabilities of scattering between directions $\hat{\varepsilon}_1' \to \hat{\varepsilon}_1$ and $\hat{\varepsilon}_2 \to \hat{\varepsilon}_2'$ are time-invariant and equal. Or since $\cos\Psi = \hat{\varepsilon}_2 \bullet \hat{\varepsilon}_2' = \hat{\varepsilon}_1' \bullet \hat{\varepsilon}_1$, we simply assume that the volume scattering phase function $\tilde{\beta}(\psi) = \tilde{\beta}(\psi; \hat{\varepsilon}_1' \to \hat{\varepsilon}_1) = \tilde{\beta}(\psi; \hat{\varepsilon}_2 \to \hat{\varepsilon}_2')$ is linear and time invariant. Under these conditions, the reciprocity relation

$$\int_{\hat{\varepsilon}\bullet\hat{n}<0} d\Omega(\hat{\varepsilon}) \int_{\text{B}} dB \left|\hat{\varepsilon} \bullet \hat{n}\right| \left[L_2(\vec{x}_{\text{B}}; \hat{\varepsilon}) L_1(\vec{x}_{\text{B}}; -\hat{\varepsilon}) - L_1(\vec{x}_{\text{B}}; \hat{\varepsilon}) L_2(\vec{x}_{\text{B}}; -\hat{\varepsilon}) \right] = \int_{\Xi} d\Omega(\hat{\varepsilon}) \int_{\text{V}} dV \left[L_2(\vec{x}; -\hat{\varepsilon}) S_1(\vec{x}; \hat{\varepsilon}) - L_1(\vec{x}; \hat{\varepsilon}) S_2(\vec{x}; -\hat{\varepsilon}) \right] \quad (1.1)$$

was shown by Case (1957) to hold between the forward and adjoint solution. The boundary **B**, in this case, is the hms at depth $z = 0$, which is located at distance Z_{hms} below the sea surface, and the volume **V** is the water column below the hms. See Mobley (1994, pp329ff) and Gordon (1985) for further discussions of the backward Monte Carlo radiative transfer solution.

We now specify the boundary conditions at **B** and reduce equation (1.1) to restrict consideration to the nadir-viewing radiance detector case [following Gordon (1985) and Mobley (1994)]. The radiance detector is located at position $\vec{x}_0$ in the boundary **B**, it is pointed towards nadir and has a solid angle acceptance $\Omega_{\text{FOV}} = 2\pi(1 - \cos\theta_{\text{FOV}}')$. A forward-solution upwelling photon arriving at the detector's boundary location $\vec{x}_0$ will be detected only if $1 \le \hat{\varepsilon}_2' \bullet \hat{z} < \cos\theta_{\text{FOV}}'$ (Fig. 1.1).

Adjoint Solution (Case 1, Fig. 1.1b)

A photon is emitted from a source at $\vec{x}_0$ in direction $\hat{\varepsilon}_1' = -\hat{\varepsilon}_2' \in \Omega_{\text{FOV}}$. On reaching the interaction location, the photon is scattered through angle ψ into direction $\hat{\varepsilon}_1 = -\hat{\varepsilon}_2$ and proceeds upward to the hms boundary **B**.

1. $L_1(\vec{x}_{\text{B}}; -\hat{\varepsilon})$ is upwelling radiance in direction $-\hat{\varepsilon}$ in **B** at distance r_{B} from $\vec{x}_0$. $L_1(\vec{x}_{\text{B}}; -\hat{\varepsilon})$ is the 3-dimensionally varying vector field to be determined by the backward MC experiments. Photons incident on **B** from below are not allowed to cross, or be reflected from, the boundary.
    i. In 2-dimensional polar coordinates in **B**, at any radial position $\vec{r}_{\text{B}} = (r_{\text{B}}, \phi_{\vec{r}_{\text{B}}})$ we may express the 3-D photon path direction incident from below on B as $-\hat{\varepsilon} = (1, \theta', \phi)$ in global coordinates translated to $\vec{r}_{\text{B}}$, or as $\hat{\varepsilon}_r = (1, \theta', \vartheta)$

relative to $\phi_{\bar{r}_B}$, where $\vartheta = \begin{cases} \phi - \phi_{\bar{r}_B}; & \phi \geq \phi_{\bar{r}_B} \\ 2\pi + \phi - \phi_{\bar{r}_B}; \text{otherwise} \end{cases}$. For the restricted case of a nadir-directed source, $L_1(\vec{x}_B; -\hat{\varepsilon}) = L_1(r_B, \phi_{r_B}; -\hat{\varepsilon}_r)$ for a given relative azimuth ϑ is invariant with respect to ϕ_{r_B}. This allows us to rigidly rotate each position vector $\vec{x}_B$ and photon path direction $\hat{\varepsilon}_r = (1, \theta', \vartheta)$ into alignment with the global $\hat{x}$ axis and accumulate photons into discrete directional bins (HYDROLIGHT Quads), and into radial distance bins Δr_B, as a function of radial distance only (Fig. 3.1), *i.e.* as $L_1(r_B, \theta', \vartheta) \rightarrow L_{1,i,j,k} = L_1(r_B \in \Delta r_k, \mu' \in \Delta\mu_i, \vartheta \in \Delta\phi_j)$, where $\mu' = \cos\theta'$. $\Delta\mu_i$ and $\Delta\phi_j$ are the $i^{\underline{th}}$ zenith angle and $j^{\underline{th}}$ azimuth angle intervals defining quadrilateral Q_{ij} in the upper hemisphere Ξ_u, and Δr_k is the distance interval of the $k^{\underline{th}}$ radial bin in **B**.

ii. There is also left-right symmetry in that $L_1(r_B, \theta', \vartheta) = L_1(r_B, \theta', -\vartheta)$, which allows further computational economies by resolving photon counts into quads in only the half of Ξ_u where $0 \leq |\vartheta| \leq \pi$.

2. $L_1(\vec{x}_B; \hat{\varepsilon}) \equiv 0$, *i.e.* there is no radiance incident on **B** from above in the adjoint problem.

3. $S_1(\vec{x}; \hat{\varepsilon}) = \begin{cases} \Im_o \delta(\vec{x} - \vec{x}_0), \hat{\varepsilon} \in \Omega_{FOV} \\ 0, \hat{\varepsilon} \notin \Omega_{FOV} \end{cases}$, *i.e.* the only source in the adjoint problem is the analog of the radiance detector in the forward problem (below). For a point source emission limited to a solid angle $\Delta\Omega_{FOV}$, $\Im_0$ is expressed in units of radiant intensity [W sr^{-1} nm^{-1}] and total emitted radiant flux is $\Im_0 \Delta\Omega_{FOV}$ [W sr^{-1}].

Forward Solution (Case 2, Fig. 1.1a)

This is the classic, 1-dimensional radiative transfer model where the boundary conditions are the radiance distribution from above, due to direct solar irradiance and sky radiance, as transmitted through the air-sea interface, at depth $z = 0_w - Z_{hms}$, and downward to B at $z = 0$. The sea surface may be flat, or roughened with capillary waves in response to wind speed. In the present study, we found it convenient to use the widely employed, commercially licensed, HYDROLIGHT Radiative Transfer model (Mobley 1994; Mobley and Sundman 2000a) to generate the downward radiance distribution incident from above on **B** for any given solar azimuth and zenith angles (θ_o, ϕ_o), sky radiance model, and wind speed. It is possible to thus employ this easy-to-use and powerful tool, because choosing an in-water hms decouples all adjoint RT solutions from the sea surface boundary conditions. Therefore, we have that

1. $L_2(\vec{x}_B; \hat{\varepsilon}) = L_2(\vec{r}_B; \hat{\varepsilon}) = \begin{cases} 0, r \leq r_1(\phi_B), \text{ i.e. within the instrument area} \\ L_2(\hat{\varepsilon}), \text{ otherwise} \end{cases}$, for $\hat{\varepsilon} \bullet \hat{n} < 0$, is the radiance distribution incident on **B**. Where the position lies within the boundaries $r_1(\phi_B)$ of the instrument cross-section, it is zero. Elsewhere, it is the horizontally invariant radiance distribution $L_2(\hat{\varepsilon})$ calculated for the above-water radiance distribution and sea surface slope

distribution using HYDROLIGHT, as angularly discretized in the standard quads Q_{ij} of Ξ_d (Mobley 1994; Mobley and Sundman 2000a).

2. $L_2\left(\vec{x}_B;-\hat{\varepsilon}\right)$, for $\hat{\varepsilon}\bullet\hat{n}<0$ is upwelling radiance crossing **B**.
3. $S_2\left(\vec{x};\hat{\varepsilon}\right)\equiv 0$, *i.e.* there are no internal sources. We defer consideration of the effects of inelastic scattering in the present study, but a simple method for including Raman scattering is outlined at the end of this report.

With the above boundary conditions for the adjoint and forward solutions, equation (1.1) reduces to

$$\begin{array}{l}\int\limits_{\hat{\varepsilon}\bullet\hat{n}<0} d\Omega\left(\hat{\varepsilon}\right)\int\limits_{B} dB\left|\hat{\varepsilon}\bullet\hat{n}\right| L_2\left(\vec{x}_B;\hat{\varepsilon}\right)L_1\left(\vec{x}_B;-\hat{\varepsilon}\right)= \\ \int\limits_{\hat{\varepsilon}\in\Omega_{FOV}} d\Omega\left(\hat{\varepsilon}\right)\int\limits_{V} dV L_2\left(\vec{x}_B;-\hat{\varepsilon}\right)J_o\delta\left(\vec{x}-\vec{x}_0\right)\end{array}, \tag{1.11}$$

and further reduces to

$$L_2\left(\vec{x}_0;\Omega_{FOV}\right)=\frac{\int\limits_{\hat{\varepsilon}\bullet\hat{n}<0} d\Omega\left(\hat{\varepsilon}\right)\int\limits_{B} dB\left|\hat{\varepsilon}\bullet\hat{n}\right| L_2\left(\vec{x}_B;\hat{\varepsilon}\right)L_1\left(\vec{x}_B;-\hat{\varepsilon}\right)}{\Im_o\Delta\Omega_{FOV}}, \tag{1.12}$$

the desired solution for the un-shaded case.

If an opaque instrument housing occupies an area $\mathbf{B_{OBJ}}$ in **B**, the self-shaded radiance $L_2^S\left(\vec{x}_0;\vec{\Omega}_{FOV}\right)$ is determined as

$$L_2^S\left(\vec{x}_0;\vec{\Omega}_{FOV}\right)=\frac{\int\limits_{\hat{\varepsilon}\bullet\hat{n}<0} d\Omega\left(\hat{\varepsilon}\right)\left[\int\limits_{B} dB\left|\hat{\varepsilon}\bullet\hat{n}\right| L_2\left(\vec{x}_B;\hat{\varepsilon}\right)L_1\left(\vec{x}_B;-\hat{\varepsilon}\right)-\int\limits_{B_{OBJ}} dB\left|\hat{\varepsilon}\bullet\hat{n}\right| L_2\left(\vec{x}_B;\hat{\varepsilon}\right)L_1\left(\vec{x}_B;-\hat{\varepsilon}\right)\right]}{\Im_o\Delta\Omega_{FOV}}. \tag{1.13}$$

It is convenient to recast (1.13) as

$$L_2^S\left(\vec{x}_0;\Omega_{FOV}\right)=\frac{\int\limits_{\hat{\varepsilon}\bullet\hat{n}<0} d\Omega\left(\hat{\varepsilon}\right)\int\limits_{B} dB\left|\hat{\varepsilon}\bullet\hat{n}\right| F_S\left(\vec{x}_B;\hat{\varepsilon}\right)L_2\left(\vec{x}_B;\hat{\varepsilon}\right)L_1\left(\vec{x}_B;-\hat{\varepsilon}\right)}{\Im_o\Delta\Omega_{FOV}}, \tag{5.2}$$

by introducing the *shading function* $F_S\left(\vec{x};\hat{\varepsilon}\right)=0$ when a shadow is cast in direction $\hat{\varepsilon}$ on B at position $\vec{x}_B$, and if not, $F_S\left(\vec{x};\hat{\varepsilon}\right)=1$. We may use these two reciprocity solutions to correct a measured radiance for the particular shading effect as

$$L_u^{True}=\frac{L_2\left(\vec{x}_0;\Omega_{FOV}\right)}{L_2^S\left(\vec{x}_0;\Omega_{FOV}\right)}L_u^{Meas}. \tag{5.3}$$

Numerical Approximations to Reciprocity and Radiative Transfer Solutions

Discrete Forward RT Radiance Distributions

A forward radiative transfer model, whether a forward Monte Carlo Model or the HYDROLIGHT model (Mobley 1994; Mobley and Sundman 2000a), yields discrete downward radiance distributions $L_2\left(\mu_{\theta'},\phi\right)\rightarrow L_{2,i,j}=L_2\left(\mu'\in\Delta\mu_i,\phi\in\Delta\phi_j\right)$, where $\mu_{\theta'}=\cos\left(\theta'\right)$, that are invariant with horizontal

position $\vec{x}_{\mathrm{B}}$ on a plane hms, e.g. **B** (Fig. 1.1), at any depth Z_{hms}. The HYDROLIGHT model organizes $L_{2:ij}$ over the lower hemisphere (corresponding to the natural direction of flux) into a polar cap centered at zenith ($\mu_{\theta'}=1$), and a Quad array $\left(\Delta\mu_i,\Delta\phi_j\right)$ that is directly analogous to a Latitude-Longtitude coordinate system in, *e.g.*, the earth's southern hemisphere. For ease in matching the forward and adjoint solutions in reciprocity calculations, we mirror image the HYDROLIGHT digital output into the upper hemisphere (*i.e.* into a "radiometer view perspective") prior to solving the reciprocity equation.

Discrete Adjoint Monte Carlo RT Radiance Distributions

In its simplest form, an AMC RT solution is obtained by emitting a very large number of photons in randomly selected directions $\hat{\varepsilon}_{01}$, falling within the sensor FOV $\Delta\Omega_{\mathrm{FOV}}$, over a randomly generated optical pathlength dependent on the beam attenuation coefficient $c\left(\lambda,Z_{\mathrm{hms}}\right)$. A photon incident in direction $\hat{\varepsilon}_{i-1,i}$ at an interaction location $\vec{x}_i$ may either be absorbed, or scattered in direction $\hat{\varepsilon}_{i,i+1}$ toward a new interaction location at an optical distance determined as a function of $c(z,\lambda)$. The probability that the single photon interaction will be a scattering event is $\omega_{\mathrm{o}}=\hat{\omega}_{\mathrm{o}}\left(z_i+Z'_{\mathrm{hms}}\right)$, the single scattering albedo, and the probability that it will be an absorption event is $\left(1-\omega_{\mathrm{o}}\right)$. Another random number $\Re\in U[0,1]$ is generated, and if $\Re>\omega_{\mathrm{o}}$ the photon is absorbed and its ray-path trajectory ends at position $\vec{x}_i$, or else, if $\Re\le\omega_{\mathrm{o}}$ the photon is scattered and the ray-path continues in a new direction $\hat{\varepsilon}_{ij}$. Refer to ISSAMC TM Chapter 2 for a detailed description of the present implementation of interaction principles and numerical representations of IOP.

The above method of tracking each single photon path trajectory, and either scattering or absorbing the photon at each interaction location, is conceptually straightforward, but computationally inefficient. One more efficient approach suggested, e.g., by Mobley (1994; and previously by several other authors cited there) is to instead emit and track a number of "photon-packets", each of which has initial weight $W_{n0}=1$. At each i$^{\underline{\mathrm{th}}}$ interaction location $\vec{x}_i$, the photon-packet weight is reduced by the probability of absorption and its residual weight $W_{ni}=\omega_{\mathrm{o}}\left(\vec{x}_i\right)W_{n,i-1}$ survives to be scattered into a new path direction. In the adjoint solution, each photon-packet path trajectory continues in this way until it either reaches the depth of the hms boundary B, or until $W_{ni}<W_{\mathrm{MIN}}$. W_{MIN} is a pre-determined threshold [Mobley (1994) suggests $W_{\mathrm{MIN}}\approx10^{-6}$] below which a photon-packet is considered to have been completely absorbed.

The "photon-packet" construct is the only "variance reduction method" that will be employed in these Monte Carlo radiative transfer models of instrument self-shading. Some other variance reduction methods are described in Mobley (1994) and references cited there.

For an arbitrary viewing direction relative to nadir, a photon packet residual weight W_{nI} reaching B, after a total of *I* interactions within B-Cell ΔB_{km} (Fig. 3.1) and intersecting the surface from below in direction $\left(\mu_{\theta'},\phi\right)$ is added to the accumulated weights in the appropriate Photon-Weight Tensor $W_{1;ijkm}\left[\mu_{\theta'}\in\Delta\mu_i,\phi\in\Delta\phi_j\right]$. In the azimuthally symmetric nadir-viewing case, the photon weight and

direction vector is rigidly rotated and all photons packet weights are accumulated into the reduced tensor $W_{1;ijk1}$ in B-cells of the sector $\Delta\phi_{\mathrm{B},1}$ containing the +x-axis. Geometric relationships implemented for this transformation are described in detail in Chapter 1 of the ISSAMC TM.

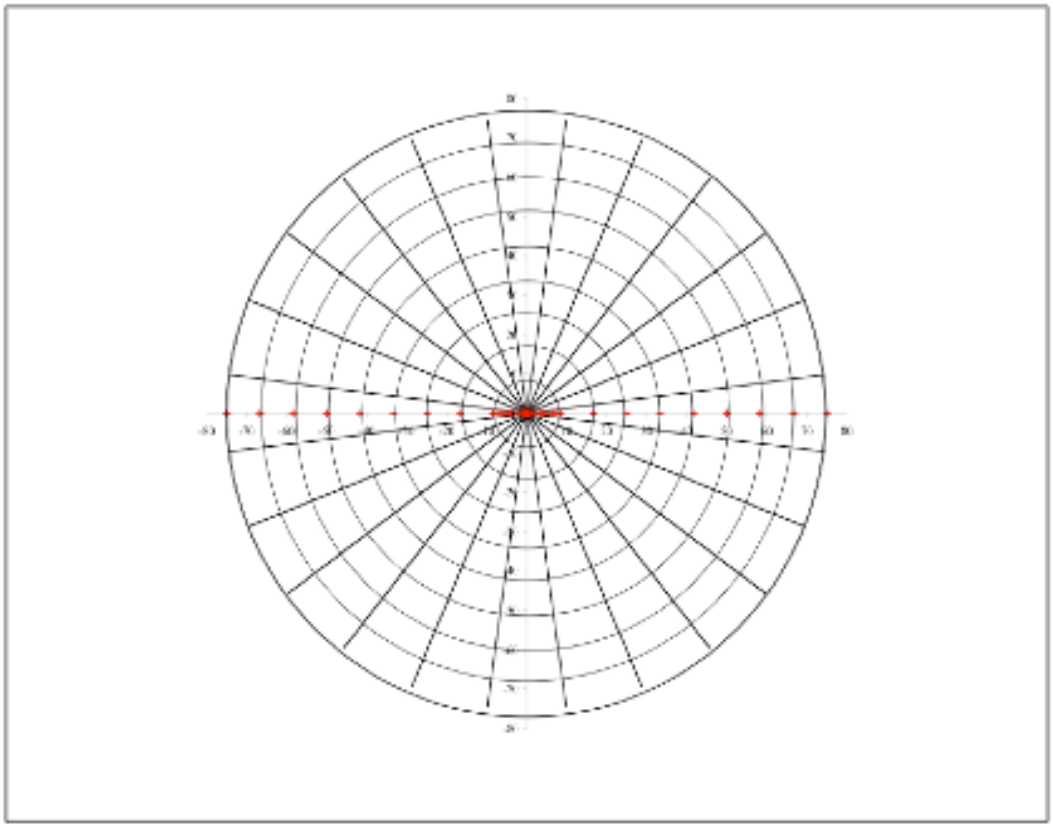

Figure 3.1: The polar coordinate "B-Cell Grid" in the horizontal-monitoring-surface **B** (Fig. 1.1). The default B-Cell layout consists of 24 azimuth sectors of width $\Delta\phi_{\mathrm{B}} = 15°$ (matching the default in the HYDROLIGHT Quad layout). Cell radial boundaries expand quasi-logarithmically with increasing distance from the origin, and by default the outermost of 37 limits $r_{\mathrm{B},37}^{\mathrm{Lim}}(\lambda, Z_{\mathrm{hms}}) = \dfrac{10}{c(\lambda, Z_{\mathrm{hms}})}$ m, where $c(\lambda, Z_{\mathrm{hms}})$ is the beam attenuation coefficient at wavelength λ and the geometric depth of **B**. Each B-Cell ΔB_{km}, located in azimuth sector $\Delta\phi_{\mathrm{B}m}$ between radii $r_{\mathrm{B}k}^{\mathrm{Lim}}$ and $r_{\mathrm{B};k-1}^{\mathrm{Lim}}$, contains an AMC radiance Quad $L_{1;ijkm}$ (a matrix element of 4 dimensional tensor array). Due to azimuth symmetry in the nadir-viewing case, however, $L_{1;ijkm}$ is obtained through rigid rotation of the Quad $L_{1;ijk1}$ (a 3-D tensor) from sector $\Delta\phi_{\mathrm{B}1}$. The downwelling radiance Quad $L_{2;ij}$ from the forward RT model (i.e. HYDROLIGHT in the present study) applies to all B-Cell locations in the grid.

We will now relate the Photon-Weight Tensor $W_{1;ijk1}$ to the radiance tensor $L_{1;ijk1}$, and by rigid rotation to $L_{1;ijkm}$. A total of N_p photon packets, each of initial weight $w_p = 1$, are emitted from the point source within solid angle $\Delta\Omega_{FOV}$ and are associated with an arbitrary constant $\Im_0$ representing source radiant intensity [W sr^{-1} nm^{-1}]. Thus, the radiant flux associated with each unit photon weight is

$$\delta\Phi_p = \frac{\Im_0 \Delta\Omega_{FOV}}{N_p}, \text{ [W nm}^{-1}\text{]}, \tag{3.3}$$

and the radiant flux represented by the sum of accumulated fractional packet weights in the photon packet weight tensor element $W_{1;ijkm}$ is, therefore,

$$\Phi_{1;ijkm} = W_{1;ijkm}\delta\Phi_p = W_{1;ijkm}\frac{\Im_0 \Delta\Omega_{FOV}}{N_p} \text{ [W nm}^{-1}\text{]}. \tag{3.4}$$

Equation (3.4) represents the radiant flux (power) accumulated within a Quad Q_{ij} solid angle $\Delta\Omega_{ij}$ and **B**-cell of projected area $\bar{\mu}_i \Delta B_{km}$. Therefore, the radiance and photon packet weight tensor elements are related as

$$L_{1;ijkm} = \frac{\Phi_{1;ijkm}}{\bar{\mu}_i \Delta B_{km} \Delta\Omega_{ij}} = \frac{W_{1;ijkm}\Im_0 \Delta\Omega_{FOV}}{\bar{\mu}_i \Delta B_{km} \Delta\Omega_{ij} N_p} \text{ [W m}^{-2}\text{ sr}^{-1}\text{ nm}^{-1}\text{]}. \tag{3.5}$$

Similarly, the radiance and photon packet weight matrices of the polar cap are related as

$$L_{1;I_Q \bullet km} = \frac{W_{1;I_Q \bullet km}\Im_0 \Delta\Omega_{FOV}}{\bar{\mu}_{I_Q} \Delta B_{km} \Delta\Omega_{I_Q \bullet} N_p}. \tag{3.6}$$

In the general case (above), photon weights are separately collected into Quads within each individual B-cell of area ΔB_{km}. To take advantage of ϕ_B-symmetry of adjoint radiance $L_1(\mu_{\theta'}, \phi - \phi_B; r_B, \phi_B)$ in the restricted case of a nadir-viewing sensor, we express the azimuth direction of a photon packet of fractional weight δw_p incident on **B** at position (r_B, ϕ_{r_B}) in direction $(\mu_{\theta'}, \phi)$ as

$$\vartheta = \phi - \phi_B. \tag{3.7}$$

and collect all photon packet weights incident within an annular ring of M_B B-cells ΔB_{km} into the Quad sums $W_{1;ijk\bullet}$. The Quad accumulated weights $W_{1;ijk\bullet}$ are then assigned to the Quad ΔB_{k1}, because within that B-cell $\vartheta = \phi$, and scaled as

$$W_{1;ijk1} = \frac{W_{1;ijk\bullet}}{M_B} \tag{3.8}$$

to account for the difference in area ΔB_{k1} and that of the entire annular ring of **B**-cells with which it is associated. The Quad photon packet weights for the remaining **B**-cells ΔB_{km} centered at each ϕ_{Bm}, $m > 1$, are then determined as

$$W_{1;ijkm} = W_{1;i,p(j,m),k1} \tag{3.9}$$

where the rotational permutation index

$$p(j,m)=\begin{cases}1+j-m; & m\le j\\ \mathrm{M_Q}+1+j-m; & m>j\end{cases} \tag{3.10}$$

accounts for rigid rotation of the scaled accumulated photon weight Quads from azimuth sector 1 to each m^{th} sector, where $\mathrm{M_B}$ is the total number of sectors, i.e. $\Delta\phi_{\mathrm{B}}=\dfrac{2\pi}{\mathrm{M_B}}$. The scaling of equation (3.8) applies as well to the polar cap photon-packet weights $W_{1;I_Q\bullet k1}$, which has no $\phi_{\mathrm{B}m}$ dependence, *i.e.* $W_{1;I_Q\bullet km}=W_{1;I_Q\bullet k1}\forall m$.

Numerical Reciprocity Solutions Without Shadows

We may approximate the solution to (1.12) in discrete numerical form as

$$L_2^{\mathrm{FOV}}\cong\frac{1}{\Im_0\Delta\Omega_{\mathrm{FOV}}}\left\{\bar{\mu}_{I_Q}\Delta\Omega_{I_Q\bullet}L_{2;I_Q\bullet}\sum_{k=1}^{\mathrm{K_B}+1}L_{1;I_Q\bullet k1}\sum_{m=1}^{\mathrm{M_B}}\Delta B_{km}+\sum_{i=1}^{\mathrm{I_Q}-1}\bar{\mu}_i\sum_{j=1}^{\mathrm{J_Q}}\Delta\Omega_{ij}\sum_{k=1}^{\mathrm{K_B}+1}\sum_{m=1}^{\mathrm{M_B}}\Delta B_{km}L_{2;ij}L_{1;i,p(j,m),k,1}\right\},\tag{5.4}$$

where the first term in brackets represents the contributions of the polar caps, and the second term represents the contributions from the remaining FRT and AMCRT quads.

The zero-azimuth quads for the FRT and AMCRT radiance distributions, $\bar{\phi}_1=0$ and $\bar{\vartheta}_1=0$ are aligned, respectively, with the zero-azimuth sectors of the B-cells, $\bar{\phi}_{\mathrm{B},1}=0$, and since we choose an equal number of azimuth sectors in each, i.e. $\left[\mathrm{M_B}=\mathrm{J_Q}\right]$, the 3 are aligned when $i=m=1$. The azimuths ϕ_j of the FRT radiance quads $L_{2;ij}$ remain fixed in global coordinates as we sum through the $\mathrm{M_B}$ azimuths sectors of B-Cells. The AMCRT radiance distribution must be rigidly rotated such that $\bar{\vartheta}_1=0$ when $\bar{\phi}_j=\bar{\phi}_{\mathrm{B},m}$. This rigid rotation of the AMCRT radiance distribution $L_{1;i,p(j,m),k,0}$ is implemented using the rotational permutation index defined in equation (3.10), and repeated here as

$$p(j,m)=\begin{cases}1+j-m; & m\le j\\ \mathrm{M_B}+1+j-m; & m>j\end{cases}.$$

Substituting from (3.1), and (3.5) through (3.10), we rewrite (5.4) in terms of the total number $\mathrm{N_p}$ of photon packets emitted and the photon packet weight accumulation tensor $W_{1;ijkm}$ as

$$L_2^{\mathrm{FOV}}=\frac{L_{2;\mathrm{I_Q}\bullet}\sum_{k=1}^{\mathrm{K_B}+1}W_{1;\mathrm{I_Q}\bullet k\bullet}}{\mathrm{N_p}}+\frac{\sum_{i=1}^{\mathrm{I_Q}-1}\sum_{j=1}^{\mathrm{J_Q}}L_{2;ij}\sum_{k=1}^{\mathrm{K_B}+1}\sum_{m=1}^{\mathrm{M_B}}W_{1;i,p(j,m),k\bullet}}{\mathrm{M_B}\mathrm{N_p}}.\tag{5.5}$$

In the double summation over i and j, each quad-averaged radiance $L_{2;ij}$ is weighted by the same double summation as

$$L_{2;ij}\sum_{k=1}^{\mathrm{K_B}+1}\sum_{m=1}^{\mathrm{M_B}}W_{1;i,p(j,m),k\bullet},$$

and since for each *j*, the rotational shift index p(j,m) takes on all values in the range from 1 to M_B, we have that

$$\sum_{m=1}^{M_B} W_{1;i,p(j,m),k\bullet} = \sum_{m=1}^{M_B} W_{1;i,m,k\bullet} .$$

Therefore, we introduce the *unshaded weighting vector*

$$U_i = \frac{\sum_{k=1}^{K_B+1}\sum_{m=1}^{M_B} W_{1;i,p(j,m),k\bullet}}{M_B N_P} = \frac{\sum_{k=1}^{K_B+1}\sum_{m=1}^{M_B} W_{1;i,m,k\bullet}}{M_B N_P}, \quad i < I_Q , \tag{5.6}$$

and for the polar caps

$$U_{I_Q} = \frac{\sum_{k=1}^{K_B+1} W_{1;I_Q\bullet k\bullet}}{N_P} , \tag{5.7}$$

and rewrite (5.5) as

$$L_2^{FOV} = \sum_{i=1}^{I_Q} U_i L_{2;i\bullet} , \tag{5.8}$$

where for $i < I_Q$,

$$L_{2;i\bullet} = \sum_{j=1}^{J_Q} L_{2;ij} .$$

In other words, absent the 3-D effects associated with shadows, the net AMCRT weighting functions are reduced to the unshaded weighting vector $\vec{U}$, the elements of which, U_i, vary only with zenith angle.

*Numerical Reciprocity Solutions With Shading by Objects In and Above **B***

The numerical representation of (5.2) that includes the distribution of radiance that would be shaded in **B** by 3-D objects in and above the plane is,

$$L_2^{FOV,S} \cong \frac{\bar{\mu}_{I_Q}\Delta\Omega_{I_Q\bullet} L_{2;I_Q\bullet} \sum_{k=1}^{K_B+1} L_{1;I_Q\bullet k1} \sum_{m=1}^{M_B} F_{S;I_Q\bullet km}\Delta B_{km}}{\Im_0 \Delta\Omega_{FOV}} + \frac{\sum_{i=1}^{I_Q-1}\bar{\mu}_i \sum_{j=1}^{J_Q}\Delta\Omega_{ij}\sum_{k=1}^{K_B+1}\sum_{m=1}^{M_B} F_{S;ijkm}\Delta B_{km} L_{2;ij} L_{1;i,p(j,m),k,1}}{\Im_0 \Delta\Omega_{FOV}} . \tag{5.9}$$

By the same substitutions used to express (5.4) as (5.5)

$$L_2^{FOV,S} = \frac{L_{2;I_Q\bullet}\sum_{k=1}^{K_B+1}\sum_{m=1}^{M_B} F_{S;I_Q\bullet km} W_{1;I_Q\bullet k\bullet}}{M_B N_p} + \frac{\sum_{i=1}^{I_Q-1}\sum_{j=1}^{J_Q} L_{2;ij}\sum_{k=1}^{K_B+1}\sum_{m=1}^{M_B} F_{S;ijkm} W_{1;i,p(j,m),k\bullet}}{M_B N_p} \tag{5.10}$$

for this general case.

For a 2-dimensional shading object that is co-planar with **B**, (5.9) reduces to

$$L_2^{\mathrm{FOV,S}} = \frac{L_{2;\mathrm{I_Q}\bullet}\sum_{k=1}^{\mathrm{K_B}+1}\sum_{m=1}^{\mathrm{M_B}} F_{\mathrm{S};\bullet\bullet km} W_{1;\mathrm{I_Q}\bullet k\bullet}}{\mathrm{M_B N_p}} + \frac{\sum_{i=1}^{\mathrm{I_Q}-1}\sum_{j=1}^{\mathrm{J_Q}} L_{2;ij}\sum_{k=1}^{\mathrm{K_B}+1}\sum_{m=1}^{\mathrm{M_B}} F_{S;\bullet\bullet km} W_{1;i,p(j,m),k\bullet}}{\mathrm{M_B N_p}}, \quad (5.11)$$

i.e. the shading function $F_{S;\bullet\bullet km}$ blocks incident radiance $L_{2;ij}$ equally from all Quad directions $\left(\bar{\mu}_i, \bar{\phi}_j\right)$, and its magnitude is $F_{S;\bullet\bullet km} = 1 - \frac{\Delta A_{km}^{\mathrm{OBJ}}}{\Delta B_{km}}$ where $\Delta A_{km}^{\mathrm{OBJ}}$ is the fractional area of the object that overlaps **B**-cell ΔB_{km}. For a shading object of fixed shape and orientation relative to the aperture, this simplification allows us to introduce a *shadow-weighting matrix* $\underset{\sim}{S}^{\mathrm{OBJ}}$ with elements

$$S_{ij}^{\mathrm{OBJ}} = \frac{\sum_{k=1}^{\mathrm{K_B}+1}\sum_{\mathrm{m}=1}^{\mathrm{M_B}} F_{S;\bullet\bullet km} W_{1;i,p(j,m),k\bullet}}{\mathrm{M_B N_p}}, \quad (5.12)$$

and for the polar cap

$$S_{\mathrm{I_Q}\bullet}^{\mathrm{OBJ}} = \frac{\sum_{k=1}^{\mathrm{K_B}+1} W_{1;I_Q\bullet k\bullet}\sum_{m=1}^{\mathrm{M_B}} F_{S;\bullet\bullet km}}{\mathrm{M_B N_p}}. \quad (5.13)$$

Substituting from (5.12) and (5.13) we may now rewrite (5.10) for the shading effect of this particular 2-D object and any incident radiance distribution as

$$L_2^{\mathrm{FOV,S}} = S_{\mathrm{I_Q}\bullet}^{\mathrm{OBJ}} L_{2;\mathrm{I_Q}\bullet} + \sum_{i=1}^{\mathrm{I_Q}-1}\sum_{j=1}^{\mathrm{J_Q}} S_{ij}^{\mathrm{OBJ}} L_{2;ij}. \quad (5.14)$$

Equations (5.12) through (5.14) used to determine the upwelling radiance self-shading by a MOBY radiometric head standoff boom, for example, given the AMC solution for the appropriate Z_{hms} and a particular IOP profile. This formulation allows us to determine shadow-weighting matrices $S_{ij}^{MOBY,IOP}$ and $S_{\mathrm{I_Q}\bullet}^{\mathrm{MOBY,IOP}}$ for a relatively small number of IOP combinations, and interpolating solutions to (5.14) to determine the L_{u} self-shading correction for incident radiance distribution $L_{2;ij}$ and IOP corresponding to a particular MOBY measurement. In essence, the initial HYDROLIGHT solution for $\bar{\phi}_1 = \phi_0 = 0$ is rotated according to $L_{Temp} = L_{2;i,,J_{\mathrm{Q}}}$, and for j = MB down to j = 2, set $L_{2;i,j} = L_{2;i,,j-1}$, and finally $L_{2;i,1} = L_{Temp}$, and the shifted downward radiance distribution is substituted in (5.14) to determine the shading effect at the new solar azimuth. This approach is enabled by the choice we made to rotate the HYDROLIGHT azimuth coordinates relative to the AMC instrument orientation azimuth coordinates [in the ISSAMC TM, see the discussion and footnote associated with equations (4.3) and (4.4)], rather than following the usual convention of expressing azimuth relative to the solar direction.

Shadowing by the MOBY Anti-Fouling Tube Assembly

The influence of shading objects below the horizontal monitoring surface **B** must be determined in the course of the Adjoint Monte Carlo solution. In the general such case, any photon packet trajectory that encounters such an object and continues to reach B must be flagged and accumulated in a full 4-D tensor. If however, the object consists of a cylinder that is coaxial with the z-axis, then the azimuthal symmetry of the nadir-viewing geometry is preserved and it is simply necessary to accumulate two 3-tensors: one accumulating all photon packet weights that reach B (the unshaded case) and another accumulating only those packet weights that do not intersect the cylinder. The Anti-Fouling Tube (AFT) used on the MOBY upwelling radiance sensors meets these latter criteria, and we develop the shading solution here, and include it in the standard Adjoint Monte Carlo solutions for MOBY results presented in this report.

The MOBY AFT is a cylindrical tube of radius 3.015 cm and length 7.975 cm that is attached to each of the MOBY upwelling radiance sensor heads. The downward viewing entrance optics are located at the top of this cylinder and look at the water column through an aperture, with radius = 1.450 cm, in the base of the cylinder. This device contains chemicals that poison marine organisms that would otherwise attach themselves to the windows and degrade the transmission, and thus invalidate the sensor's calibration.

The AFT completely shadows the first ~8 cm of the optical path below the entrance aperture. In the adjoint Monte Carlo experiments, any photon packet that has its initial interaction within a pathlength < 8 cm, and scatters in a direction that does not clear the aperture in the cylinder's base, is effectively absorbed. Similarly, any photon packet is also lost if it initially escapes from the tube, but its trajectory subsequently intersects the tube's volume. The effects of these losses are quantified in the AMC RT software by simply flagging each photon packet that intersects the tube as "TUBED". All photon packet weights reaching **B** are accumulated into the tensor $W_{1;ijk1}$ and polar cap vector $W_{1;\mathrm{I_Q}\bullet k1}$ as before to obtain the unshaded reciprocity solution, and only those packet weights that are "NOT TUBED" are accumulated into a second tensor $W^{\mathrm{AFT}}_{1;ijk1}$ and vector $W^{\mathrm{AFT}}_{1;\mathrm{I_Q}\bullet k1}$, which are substituted in equations (5.6) through (5.8) to obtain the reciprocity solution for $L_2^{\mathrm{FOV,AFT}}$, *i.e.* radiance measured in the presence of the anti-fouling tube alone. The matrix shading function $F_{S;\bullet\bullet km}$ for 2D objects in **B**, $W^{\mathrm{AFT}}_{1;ijk1}$, and $W^{\mathrm{AFT}}_{1;\mathrm{I_Q}\bullet k1}$ are substituted in equations (5.12) and (5.13) to find the combined shadow-weighting matrix $S_{ij}^{\Sigma Objects}$ and polar cap shadow weight $S_{\mathrm{I_Q}\bullet}^{\Sigma Objects}$. The combined shadow weights, computed thus are substituted into (5.14) to solve for $L_2^{\mathrm{FOV,S}}$, and shadow corrections are applied using equation (5.3), i.e. as

$$L_{\mathrm{u}}^{\mathrm{True}} = \frac{L_2\left(\vec{x}_0;\Omega_{\mathrm{FOV}}\right)}{L_2^{\mathrm{S}}\left(\vec{x}_0;\Omega_{\mathrm{FOV}}\right)} L_{\mathrm{u}}^{\mathrm{Meas}}. \qquad (5.3)$$

Upwelling Radiance Self-Shading Model for MOBY: Homogeneous IOP (MH1)

Because inherent optical properties (IOP) are not routinely measured in conjunction with upwelled radiance measurements at the MOBY site, we must specify wavelength-dependent values of absorption and scattering coefficients that are reasonably representative of the clear ocean waters in that location.

We adopt the following criterion for estimating a representative range of IOP at the MOBY site:

1. We assume that the IOP are vertically homogeneous and that the depth of the water column is optically infinite.
2. We assume for the Case-I waters at MOBY, that the Gordon and Morel (1983) *Chl*-specific particle absorption and scattering models, and variants, as adopted as a default in the **abcase1** variant of the HYDROLIGHT model (Mobley and Sundman 2000a, 200b), will provide a reasonable starting point for simulating a range of optical property variations over both time and wavelength.
3. We will not, at least for the initial series of RT calculations, incorporate the *Chl*-dependent CDOM (yellow-substance) part of the Gordon and Morel (1983) model.
4. If we assume that wavelength dependent variations in the backscattering fraction of the particle scattering phase function, $\tilde{b}_{\mathrm{bp}}(\lambda) = \dfrac{b_{\mathrm{bp}}(\lambda)}{b_{\mathrm{p}}(\lambda)}$, may be represented as an "Angstrom-type" exponential function of wavelength, i.e. $\tilde{b}_{\mathrm{bp}}(\lambda) = \tilde{b}_{\mathrm{bp}}(\lambda_0)\left(\dfrac{\lambda}{\lambda_0}\right)^{n_{\mathrm{bp}}}$, we may vary $\tilde{b}_{\mathrm{bp}}(\lambda_0)$ and the exponent n_{bp} to examine the sensitivity of self-shading corrections to variations in wavelength dependent shapes of the scattering phase function.

Table 6.1 lists the values of *Chl*, $\tilde{b}_{\mathrm{bp}}(\lambda_0), \lambda_0 = 550$ nm, and the exponent n_{bp} to be used to determine IOP for calculating an initial set of adjoint Monte Carlo RT and forward HYDROLIGHT RT solutions, which will be joined for self-shading solutions. Values set off in square brackets in Table 6.1 represent cases that time and resources did not allow us to incorporate within the completed scope of this project.

Pure Sea Water Absorption and Scattering Properties

Absorption by pure water is implemented in the AMC RT by combining, for different spectral regions, the values reported by Pope and Fry (1997), Sogandares and Fry (1997), and Kou *et al*. (1993).

Scattering by pure seawater is taken from Morel (1974), as expanded and tabulated by Smith and Baker (1981). The scattering phase function for pure water is that published by Morel (1974).

The above specifications for the AMC RT model match those used as defaults in HYDROLIGHT, as we verified by inspecting and comparing the IOP listings in the outputs from both programs.

Chlorophyll-Specific Absorption and Scattering by Particles

As in the HYDROLIGHT model's default **abcase1** configuration, we will determine the Chl dependent particle absorption coefficient as

$$a_p(\lambda;Chl) = 0.05 A_p^{HFE}(\lambda)[Chl]^{0.65}, \quad (6.1)$$

and the particle scattering coefficient as

$$b_p(\lambda;Chl) = 0.3[Chl]^{0.62}\left(\frac{550}{\lambda}\right), \quad (6.2)$$

(Mobley and Sundman 2000a, 2000b; Gordon and Morel 1983; Morel and Maritorena 2000; Prieur and Sathyendranath 1981). In equation (6.1), the function $A_p^{HFE}(\lambda)$ is the smoothed HFE representation of *Chl*-specific absorption illustrated in Fig. 6.1.

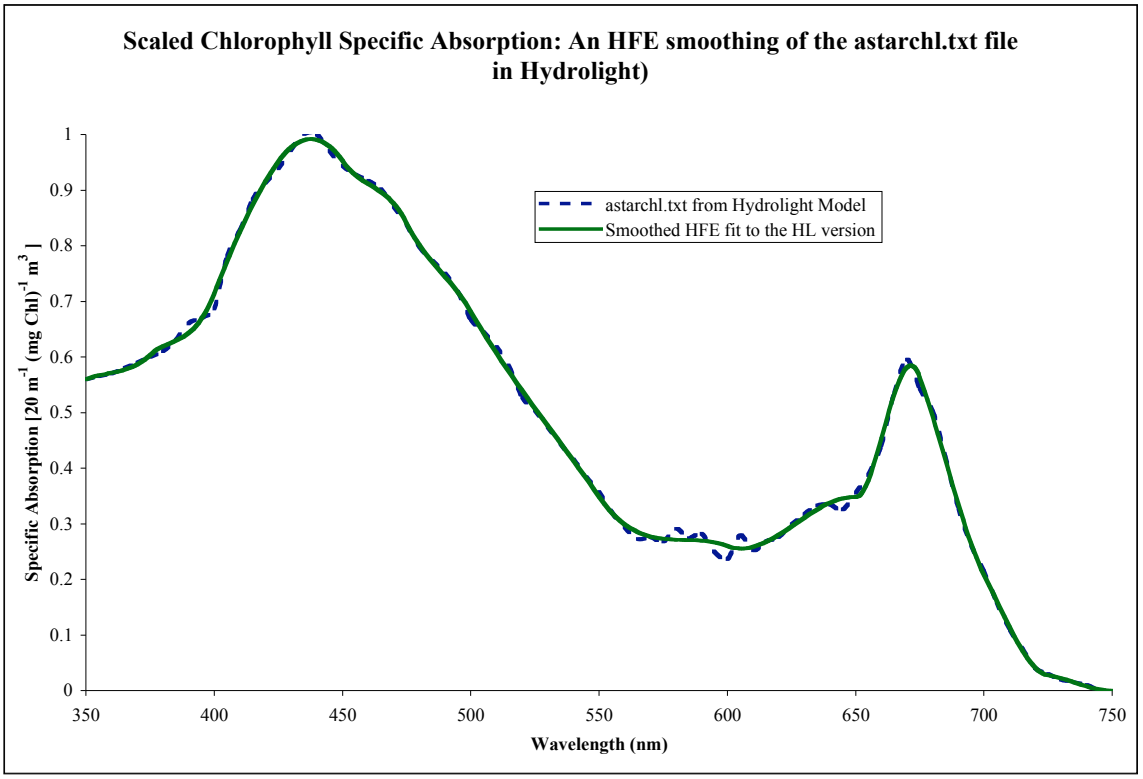

Figure 6.1. Smoothed Chlorophyll-specific absorption spectrum (scaled by a factor of 20) based on the HYDROLIGHT RT model implementation (Mobley and Sundman 2000b), which is taken in turn from Prieur and Sathyendraneth (1981).

The use of ***Chl*** as an **IOP Index** to characterize Case 1 waters is a practice introduced and popularized by Andre Morel and colleagues. The reader is cautioned that while the IOP Index *Chl* will usually be similar in magnitude to chlorophyll concentration measured by HPLC, or chlorophyll fluorescence methods, we do not expect it to be a best-fit model for that purpose. Of more import in

the present context, it is never appropriate to use either a chemically determined chlorophyll concentration, or a remote sensing algorithm fit to such data, as a basis for selecting a *Chl*-dependent MOBY self-shading model. The IOP Index *Chl* is employed here as a convenient way to specify a representative range of variations in spectral absorption and scattering coefficients for particles in Case 1 waters. These IOP are then used to generate linked sets of backward (adjoint) Monte Carlo and forward HYDROLIGHT radiative transfer models (Mobley 1994; Mobley and Sundman 2000a, 2000b) results, and resulting MOBY shadow effects/corrections. Additional research will be needed to develop a robust method of matching MOBY measured $L_u^{MOBY}(z,\lambda)$ spectra to modeled $L_u^{Model}\left(z,\lambda;Chl,\tilde{b}_{bp}\right)$, including possibly the retuning of the modeled $L_u^{Model}\left(z,\lambda;Chl,\tilde{b}_{bp}\right)$ spectral characteristics to allow closer matches to be determined. Completing that phase of the research proved beyond the limits of available time and resources in this project. At the end of this report we outline a relatively straightforward approach to addressing this aspect of the problem.

Table 6.1: MOBY Homogeneous-IOP Series-1 (MH1) Backward Monte Carlo and HYDROLIGHT RT setup parameters

Variable	Range of Values	Number of Cases	Output IOP
Solar Zenith θ_0 [deg]	0, 10, 20, 30, 40, 50, 60	7	
Wavelength λ [nm]	Min(Delta)Max = 355(5)750	80	
Chl [mg m^{-3}]	0.04, 0.05, 0.06, 0.07, 0.08, 0.09, 0.10, 0.11, 0.125, 0.15, 0.175, 0.20, 0.225, 0.25, 0.275, 0.30	16	$a_p(\lambda), b_p(\lambda)$
$\tilde{b}_{bp}(550)$	0.010, 0.015, 0.020, 0.025, 0.030	5	$\tilde{b}_{bp}(\lambda), \tilde{\beta}_p(\psi,\lambda)$
n_{bp}	0.0, [0.1*, 0.5*]	1[3]	
Nr. of 80-λ AMC runs		80 [240]	
Nr of HYDROLIGHT RT 80-λ runs (7 x 16 x 5 x 1)		560[1680]	
*Not done, and therefore, not included in the present MH1 results.			

Particle Phase Function Backscattering Fraction

The Fournier-Forand particle phase function (Fournier and Forand 1994) for the MH1 radiative transfer series will be determined using an assumed real refractive index of 1.10 and the backscattering coefficients determined using values in Table 1 and the equation

$$\tilde{b}_{bp}(\lambda) = \tilde{b}_{bp}(550)\left[\frac{\lambda}{550}\right]^{n_{bp}}. \qquad (6.3)$$

Although a capability to vary n_{bp} is included in the Monte Carlo software, and simulated 81-channel HYDROSCAT format files can be used to incorporate this feature into HYDROLIGHT runs, available resources and time limit the results presented here to cases with $n_{bp} = 0.0$ (*i.e.* a constant phase function is assumed at all wavelengths of each run). Additional runs with $n_{bp} > 0.0$ may be useful in tuning the self-shading model to improve spectral matching between measured $L_u^{MOBY}(z,\lambda)$ and modeled $L_u^{Model}\left(z,\lambda;Chl,\tilde{b}_{bp}\right)$.

The AMC and HYDROLIGHT RT models each utilize a library of Fournier-Forand (1994) functions that are indexed by specific values of $\tilde{b}_{bp}$, and each uses interpolation to determine scattering functions for intermediate normalized backscattering fractions. The numerical implementation and method of application of these phase functions differ, however, between the AMC RT (ISSAMC TM, Chapter 2) and HYDROLIGHT (Mobley and Sundman 2000b) models.

Adjoint Monte Carlo Radiative Transfer (AMCRT) for MOBY: MH1 Wavelength and IOP Variations

The objective of each individual AMC RT solution is to generate an LQr0 Polar Cap vector (nadir L_u at 37 B-Cell radii) and LQr tensor (L_u at 9 zenith angles x 24 azimuth angles x 37 B-Cell radii) for each particular combination of nadir-viewing sensor depth, Z_{hms}, wavelength λ, and IOP profiles $\left[a(z,\lambda), b(z,\lambda), \tilde{\beta}(z,\lambda,\psi)\right]$ beneath the horizontal measuring surface containing the sensor at Z_{hms}. Having assumed that MOBY is located in an optically deep, vertically homogeneous water column, we may compute an AMCRT solution for $Z_{hms} = 0$, and simply shift it downward to any other measurement depth in the water column and merge it with a corresponding (*i.e.* same wavelength and IOP specification) forward HYDROLIGHT RT L_d Quad array solution for that depth.

The AMCRT MOBY Homogeneous IOP 1 (MH1) series of adjoint radiance computations were initialized using *Chl*, and backscattering fraction at 550 nm $\left[\tilde{b}_{bp}(550)\right]$ and wavelength exponent $\left[n_{bp}\right]$, taking values specified in Table 6.1, and each program execution covered the wavelength range from 355 nm to 750 nm at 5 nm intervals. These initialization parameter values were used, as describe above, to determine the wavelength-dependent IOP $a_p(\lambda), b_p(\lambda)$ and $\tilde{b}_{bp}(\lambda)$. To complete the IOP specification, the particle scattering phase function $\tilde{\beta}_p(\psi,\lambda)$ was modeled by a Fournier-Forand function with backscattering fraction $\tilde{b}_{bp}(\lambda)$ and a refractive index of 1.10 (see above).

For each such IOP specification, the AMC RT model was run to generate photon-packet weight Quad $W_{1;ijk\bullet}\left(\lambda;Chl,\tilde{b}_{bp}\right)$ and polar cap $W_{1;I_Q\bullet k1}\left(\lambda;Chl,\tilde{b}_{bp}\right)$ arrays for the unshaded case, and $W^{AFT}_{1;ijk1}\left(\lambda;Chl,\tilde{b}_{bp}\right)$ and $W^{AFT}_{1;I_Q\bullet k1}\left(\lambda;Chl,\tilde{b}_{bp}\right)$ arrays for the AFT-shaded case, all for the single hms depth $Z_{hms} = 0$, since the results for the surface can also be applied at any other depth in a homogeneous water column.

HYDROLIGHT Forward Radiative Transfer for MOBY: MH1 Wavelength, IOP and Solar Zenith Angle Variations

The HYDROLIGHT Radiative Transfer model was used here for 1-dimensional forward computations of radiance distributions in horizontal monitoring surfaces (hms) just below the sea surface $\left(Z_{hms} = 0^w\right)$ and depths of the MOBY upwelling radiance apertures: 1.3, 5.1 and 9 m. For each Chl (IOP specification), HYDROLIGHT was run for solar azimuth $\phi_0 = 0$, and solar zenith angles $\theta_0 = 0°, 10°, 20°, 30°, 40°, 50°, \& \; 60°$. The zenith sun, $\theta_0 = 0°$, case is included to provide for a "normalized" upwelling radiance, analogous to normalized water-leaving radiance (Gordon and

Clark 1981; Morel and Gentili 1996) that may be used in methods, outlined at the end of this report, to apply the MH1 results to MOBY upwelling radiance measurements.

Although the MH1 strategy for determining $a_{\mathrm{p}}(\lambda,Chl), b_{\mathrm{p}}(\lambda,Chl)$ and $\tilde{b}_{\mathrm{bp}}(\lambda)$ is closely based on that used in HYDROLIGHT's "Gordon and Morel" classic Case1 water variant, designated **abcase1** (Mobley and Sundman 2000a, 2000b), the details of our implementation deviate enough from those in HYDROLIGHT to preclude using the ABCASE1 option directly. Instead, we generated synthetic "ac-81" files of $a(\lambda;Chl)-a_{\mathrm{w}}(\lambda)$, and $c(\lambda;Chl)-c_{\mathrm{w}}(\lambda)$, and "Hydroscat81" files of $b_{\mathrm{b}}\left(\lambda;Chl,\tilde{b}_{\mathrm{bp}}(550),n_{\mathrm{bp}}\right)$, in the formats specified for the HYDROLIGHT ***"abacbb"*** routine. Since we did not specify $n_{\mathrm{bp}}>0$, however, we did not use the synthetic "Hydroscat81" files and simply specified the constant phase function backscattering fractions in the HYDROLIGHT IOP specification form. In any case, since the MH1 cases are vertically homogeneous it is only necessary to specify the IOP at $z = 0_{\mathrm{w}}$.

The HYDROLIGHT digital output data files were parsed to extract, at each hms depth, $L_{\mathrm{u}}(Z_{hms},\lambda)$ and the downwelling diffuse and direct radiance distributions, which were combined and mirror-imaged into a "radiometer-view perspective" downwelling radiance distribution polar caps $L_{2;I_Q\bullet}\left(Z_{\mathrm{hms}},\lambda;Chl,\tilde{b}_{\mathrm{bp}},\theta_0\right)$ and Quad arrays $L_{2;ijk}\left(Z_{\mathrm{hms}},\lambda;Chl,\tilde{b}_{bp},\theta_0,\phi_0=0\right)$. Downwelling radiance distributions for other solar azimuth angles were obtained by sequentially shifting Quad values, in each solar zenith bin, to rotate the entire radiance distribution in 15-degree azimuth steps.

Results: The MH1 Reciprocity Solutions

The HYDROLIGHT downwelling radiance distributions $L_{2;ijk}\left(Z_{\mathrm{hms}},\lambda;Chl,\tilde{b}_{bp},\theta_0,\phi_0=0\right)$ were combined with AMC RT backward photon-packet weight Quad $W_{1;ijk\bullet}\left(\lambda;Chl,\tilde{b}_{\mathrm{bp}}\right)$ and polar cap $W_{1;I_Q\bullet k1}\left(\lambda;Chl,\tilde{b}_{\mathrm{bp}}\right)$ arrays for the unshaded case, and $W^{\mathrm{AFT}}_{1;ijk1}\left(\lambda;Chl,\tilde{b}_{\mathrm{bp}}\right)$ and $W^{\mathrm{AFT}}_{1;\mathrm{I_Q}\bullet k1}\left(\lambda;Chl,\tilde{b}_{\mathrm{bp}}\right)$ arrays for the AFT-shaded case, to solve the reciprocity equations (see above) at $Z_{\mathrm{hms}} = 0_{\mathrm{W}}, 1.3, 5.1, 9$ m. The output includes the spectra of unshaded upwelling radiance $L^{\mathrm{FOV}}_{2}\left(Z_{\mathrm{hms}},\lambda;Chl,\tilde{b}_{\mathrm{bp}},\theta_0\right)$, the AFT-shaded upwelling radiance $L^{\mathrm{FOV}}_{2\mathrm{S;AFT}}\left(Z_{\mathrm{hms}},\lambda;Chl,\tilde{b}_{\mathrm{bp}},\theta_0\right)$, upwelling radiance shaded by the MOBY Boom/Spar cross-section (Fig. 6.2) alone $L^{\mathrm{FOV}}_{2\mathrm{S;BS}}\left(Z_{\mathrm{hms}},\lambda;Chl,\tilde{b}_{\mathrm{bp}},\theta_0,\phi_0\right)$ and upwelling radiance shaded by the combined MOBY Boom/Spar and AFT $L^{\mathrm{FOV}}_{2\mathrm{S;Total}}\left(Z_{\mathrm{hms}},\lambda;Chl,\tilde{b}_{\mathrm{bp}},\theta_0,\phi_0\right)$ for $\phi_0 = 0°,15°,30°,\cdots,165°,180°$. HYDROLIGHT solutions always have left-right symmetry, and we averaged corresponding left-right (*i.e.* $+\phi_0 \Leftrightarrow -\phi_0$) AMC RT photon-packet weight Quads to enforce this conditions as well, so that the azimuth dependence of the Boom/Spar shading effect in the range $\phi_0 \subset [0°,-180°]$ is an identical mirror image of that in the positive azimuth semi-circle.

Spectra of AFT-only shading corrections $\dfrac{L^{\mathrm{FOV}}_{2}\left(Z_{\mathrm{hms}},\lambda;Chl,\tilde{b}_{\mathrm{bp}},\theta_0\right)}{L^{\mathrm{FOV}}_{2\mathrm{S;AFT}}\left(Z_{\mathrm{hms}},\lambda;Chl,\tilde{b}_{\mathrm{bp}},\theta_0\right)}$, truncated at 600 nm, are illustrated in Figs. 6.3a and 6.3b. In Fig. 6.3a, self-shading corrections decrease visibly with depth,

but even where the effect is largest at $\theta_0 = 10°$ the depth dependent variations do not exceed 0.25 %. Depth dependent variations of combined corrections (not shown) for *Chl* = 0.1 and $\theta_0 = 10°$ are similarly small at $|\phi_0| = 90°$, but become quite large approaching $|\phi_0| = 0°$, where at Z = 1.3 and 9 m, respective ISS corrections are 1.14 and 1.05 at 500 nm, and 1.28 and 1.13 at 550 nm. This behavior probably reflects the progressively reduced cross-sections of the MOBY spar and boom cross-section at 5.1 and 9 m. Future research on this problem should include a closer examination of the depth-sensitivity of MOBY self-shading corrections spanning more complete ranges of *Chl* and θ_0. In the remainder of this report, however, we illustrate and discuss only characteristics of results for $Z_{\text{hms}} = 0_{\text{W}}$, where the 1.3 m MOBY Boom/Spar dimensions are replicated on a hypothetical basis.

The AFT-only spectral shading corrections $\dfrac{L_2^{\text{FOV}}\left(Z_{\text{hms}},\lambda;0.10,0.015,\theta_0\right)}{L_{2\text{S;AFT}}^{\text{FOV}}\left(Z_{\text{hms}},\lambda;0.10,0.015,\theta_0\right)}$ for $\theta_0 = 30°$ and $\theta_0 = 60°$ (Fig. 6.3a) closely track each other near 1.01 between 355 nm and 500 nm, increasing to about 1.02 adjustments at 550 nm, and then sharply increasing to much larger corrections (effects) at wavelengths $\gtrsim 565$ nm; apparent noise levels (fluctuation amplitudes) are 0.001 to 0.002, increases to ~0.003 near 550 nm. At $\theta_0 = 10°$, the correction ranges between ~1.01 and ~1.02 below 500 nm, and increases to ~1.04 at 550 nm; apparent noise levels (fluctuation amplitudes) are approximately ~0.002 to ~0.003 below 500 nm, but increase to between ~0.005 and ~0.01 near and above 550 nm.

Fig. 6.3b compares changes in the AFT-shading correction spectra $\dfrac{L_2^{\text{FOV}}\left(0_{\text{W}},\lambda;Chl,0.015,\theta_0\right)}{L_{2\text{S;AFT}}^{\text{FOV}}\left(0_{\text{W}},\lambda;Chl,0.015,\theta_0\right)}$ for $\theta_0 = 10°, 30°, \& 60°$ at *Chl* values of 0.1, 0.2 and 0.3. Below 500 nm, the AFT-correction factors monotonically increase by ~0.002 per 0.1 increase in *Chl* at $\theta_0 = 30°, \& 60°$, and by ~0.005 per 0.1 *Chl* step at $\theta_0 = 10°$; at wavelengths >500 nm, spectral deviations in AFT-corrections at different *Chl* IOP-Index values are present but are not visually distinct from noise fluctuations.

We now define the combined total MOBY Boom/Spar & AFT Instrument Self Shading factor as

$$R_{\text{ISS}}^{\text{MOBY}}\left(Z_{\text{hms}},\lambda;Chl,\tilde{b}_{\text{bp}},\theta_0,\phi_0\right) \equiv \frac{L_2^{\text{FOV}}\left(Z_{\text{hms}},\lambda;Chl,\tilde{b}_{\text{bp}},\theta_0\right)}{L_{2\text{S;Total}}^{\text{FOV}}\left(Z_{\text{hms}},\lambda;Chl,\tilde{b}_{\text{bp}},\theta_0,\phi_0\right)}.$$

Fig. 6.3c illustrates 3 families of curves for solar azimuth angles $|\phi_0| = 0°, 15°, 30°, 90°, 120°, \& 180°$ for the self-shading factors $R_{\text{ISS}}^{\text{MOBY}}\left(0_{\text{W}},\lambda;Chl,0.10,0.015,\phi_0\right)$ at solar zenith angles $\theta_0 = 10°$ (Blue), 30° (Green), & 60° (Red). Shown for comparison are AFT-shading factors from Fig. 2.3a for $\theta_0 = 10°$ (Solid Grey), & 60° (Dashed Grey). Note the increase in scale from a maximum of 1.05 in Figs. 6.3a and 6.3b to 1.20 in 6.3c. At $\left(\theta_0,|\phi_0|\right) = \left(10°,0°\right)$ the minimum shading factor near 440 nm is ~1.07, increasing to ~1.17 at 500 nm and is off-scale at 550 nm. Corrections for $\left(10°,|\phi_0|\right)$ remain ≥ 1.05 at 500 nm and 550 nm for $|\phi_0| = 15°, \& 30°$, and become at best, marginally acceptable at higher solar azimuths. At $\theta_0 = 30°, \& 60°$, $|\phi_0| > 30°$ and $\lambda \leq 500$ nm, correction spectra $R_{\text{ISS}}^{\text{MOBY}}\left(0_{\text{W}},\lambda;0.10,0.015,\theta_0,\phi_0\right)$ remain between 1.01 and 1.02, while the envelope widens to span from ~1.02 to ~1.04 at 550 nm.

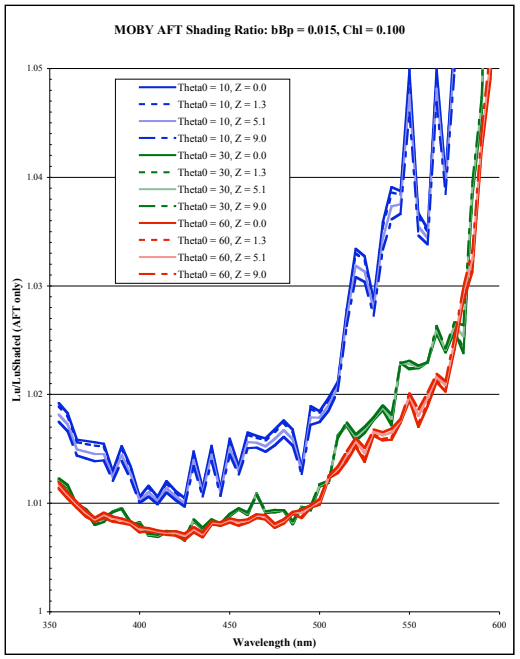

a.

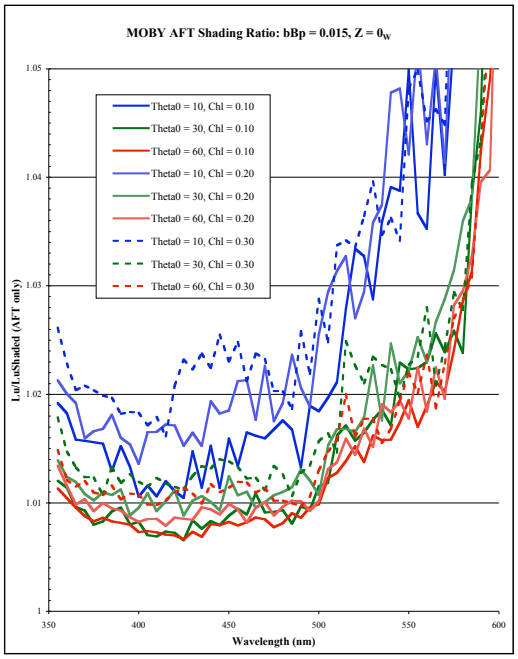

b.

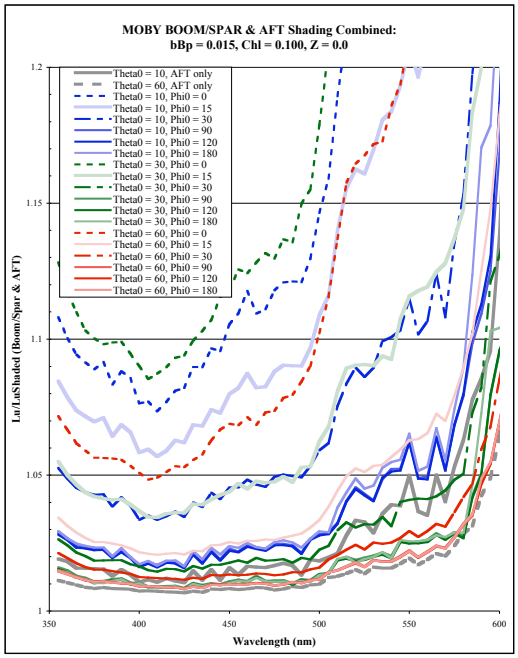

c.

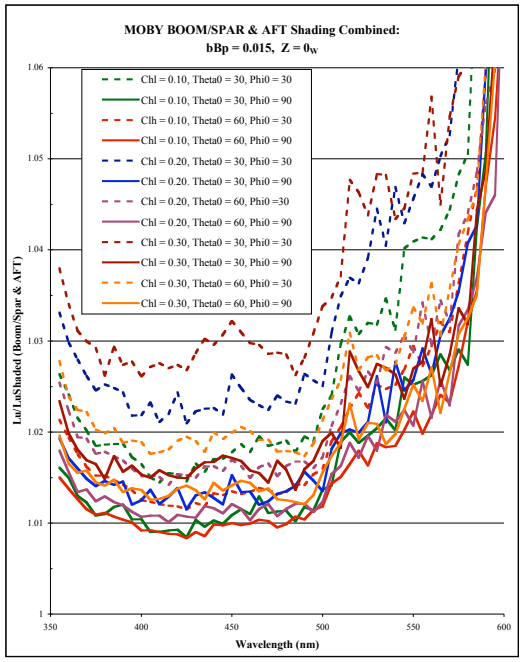

d.

Fig. 6.3: Spectral variations of the AFT shading factor with solar zenith angle and depth (**a**) and Chl (**b**). Lower Panels: Spectral variations of Total MOBY Boom/Spar & AFT shading factor with solar zenith and azimuth angles (**c**), and with Chl at four solar (zenith, azimuth) combinations (**d**).

Fig. 6.3d compares 6 sets of 2 $R_{\mathrm{ISS}}^{\mathrm{MOBY}}\left(0_{\mathrm{W}},\lambda;Chl,0.015,\theta_0,\phi_0\right)$ spectra, at $\left|\phi_0\right|=30°$ & $90°$ with $\theta_0 = 30°$ or $60°$ and $Chl = 0.10, 0.20,$ & 0.30 . A separate color is used to show each pair in the set, with

a dash line for $\theta_0 = 30°$ and a solid line for $\theta_0 = 60°$. In each (same color) pair, the spectrum of corrections (dash line) for $|\phi_0| = 30°$ is significantly larger than that (solid line) for $|\phi_0| = 90°$, as one would expect. At each fixed combination of $(\theta_0, |\phi_0|)$, the spectra also increase significantly with increasing *Chl*; this is most easily seen by inspecting the green, blue and red dash curves (third, second and first from the top at 520 nm), which correspond to $(\theta_0, |\phi_0|) = (30°, 30°)$ spectra at $Chl = 0.10, 0.20, \& 0.30$, respectively.

Figure 6.4 illustrates the variations with solar azimuth ϕ_0 of $R_{\rm ISS}^{\rm MOBY}(0_{\rm W}, 400; Chl, 0.015, \theta_0, \phi_0)$ at $\theta_0 = 0°, 10°, 20°, 30°, 40°, 50°, \& 60°$ with *Chl* = 0.05 (6.4a), 0.10 (6.4b), 0.20 (6.4c) and 0.30 (6.4d). The curves shown here are truncated at $\phi_0 = 345°$, but for completeness we could attach the value at $\phi_0 = 0°$ to complete the azimuthally symmetric curves to $\phi_0 = 360°$. As expected, corrections increase monotonically with *Chl* (absorption). For the "usable" sun-angle range $\theta_0 \geq 30°$ and $|\phi_0| > 45°$, sensitivity to solar azimuth is very weak, although the slight increase in shadow effects of the boom end as solar azimuth approaches $|\phi_0| = 180°$ becomes more apparent as *Chl* increases. In this "usable" solar zenith and azimuth range, the full range of expected Chl values increases the "baseline corrections" from ~1.007 to ~1.013, and increases the range of θ_0 dependence at $|\phi_0| = 180°$ from <0.001 at *Chl* = 0.05 (Fig. 6.4a) to ~0.05 at *Chl* = 0.30 (Fig.6.4d).

Figs. 6.5a and 6.5b are similar in format to Fig. 6.4, and compare azimuth variations of $R_{\rm ISS}^{\rm MOBY}(0_{\rm W}, \lambda; Chl, 0.010, \theta_0, \phi_0)$ at wavelengths $\lambda = 400, 490, 550, \& 600$ nm and $Chl = 0.10 \& 0.20$, at $\theta_0 = 30°$ (Fig. 6.5a) and $\theta_0 = 60°$ (Fig. 6.5b). In both θ_0 cases, shading corrections increase by ~0.003 at 400 nm and 490 nm, and ~0.006 at 600 nm, but decrease by ~0.005 to ~0.009 at 550 nm. To evaluate this discrepancy, we examine in Fig. 6.6 the full spectra of shading factors $R_{\rm ISS}^{\rm MOBY}(0_{\rm W}, \lambda; Chl, 0.010, 30°, 180°)$ for $Chl = 0.10 \& 0.20$ (corresponds to Fig. 6.5a). Below ~515 nm a *Chl*-dependent increase in self-shading $(\Delta R_{\rm ISS}^{\rm MOBY} \sim 0.004 \text{ per } \Delta Chl = 0.10)$ emerges clearly above the noise of the 10^6 Photon-Packet Monte Carlo solutions, but as wavelength increases from that point, absorption by water rises sharply and the fluctuation amplitudes in the AMC RT solutions increases $\Delta R_{\rm ISS}^{\rm MOBY}$ noise above ~0.005 accordingly. Fig. 6.5b shows similar behavior for $\theta_0 = 60°$, but at both zenith angles we must conclude that the consistency of apparent *Chl*-dependent increases at 600 nm are purely coincidental.

In Figs. 6.5c and 6.5d we compare ϕ_0 distributions of $R_{\rm ISS}^{\rm MOBY}(0_{\rm W}, \lambda; 0.10, \tilde{b}_{\rm bp}, \theta_0, \phi_0)$ at $\lambda = 400, 490, 550, \& 600$ nm, $\theta_0 = 30°$ (Fig. 6.5c) and $\theta_0 = 60°$ (Fig. 6.5d), in this case to evaluate sensitivity to backscattering fractions $\tilde{b}_{\rm bp} = 0.010, 0.020, \& 0.030$ at each zenith angle. We again see small (~0.001 to ~0.003) $\tilde{b}_{\rm bp}$-dependent increases in self-shading at 400 and 490 nm, but in both figures, apparent sensitivity to $\tilde{b}_{\rm bp}$ is erratic at 550 nm and 600 nm, where the absorption induced increasing uncertainty of the Monte Carlo solution (Fig. 6.6) masks this effect.

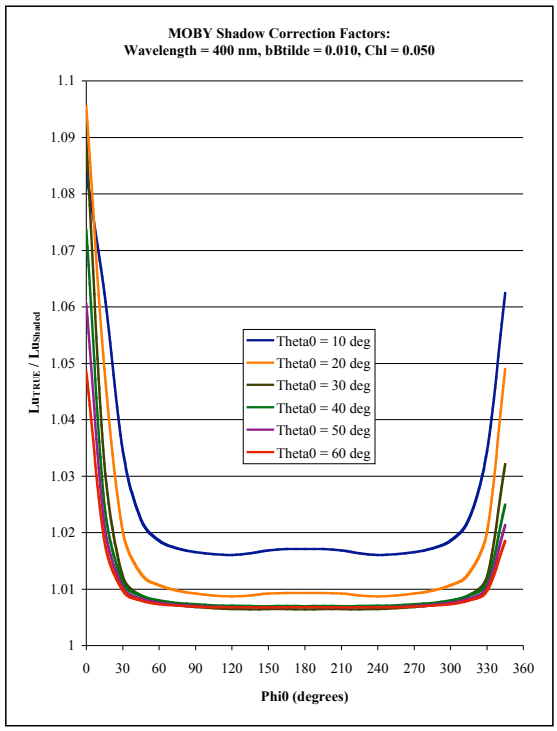

a.

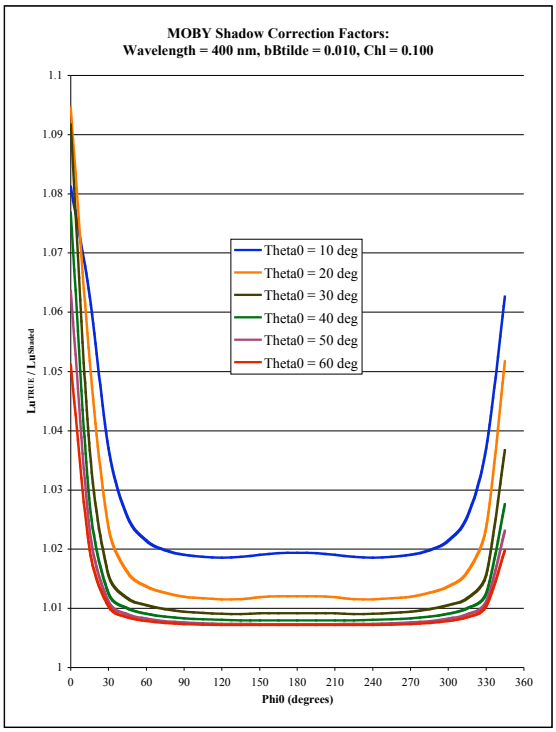

b.

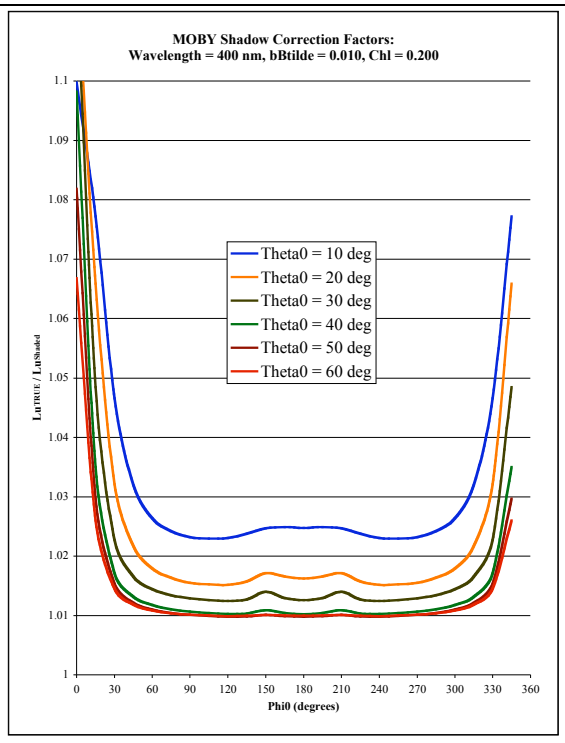

c.

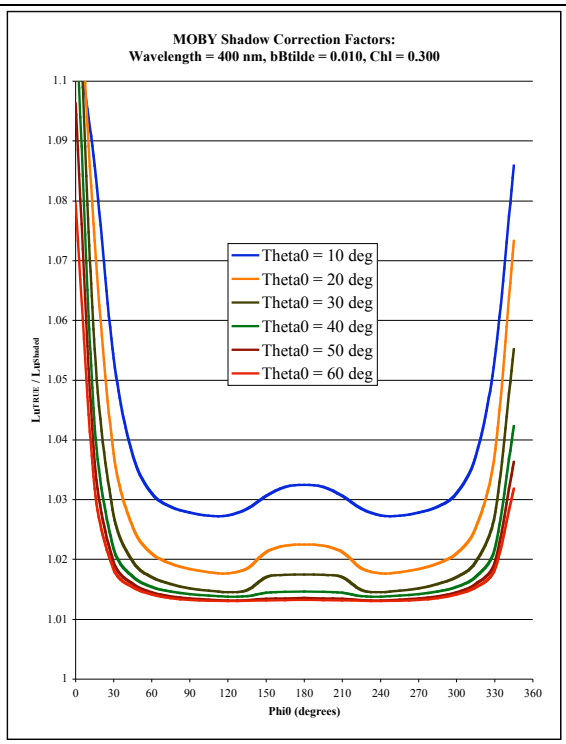

d.

Fig. 6.4: Evolution of MOBY self-shading corrections with solar azimuth at 400 nm ($z = 0_w$); variations with solar zenith angle and the "Chl" IOP index.

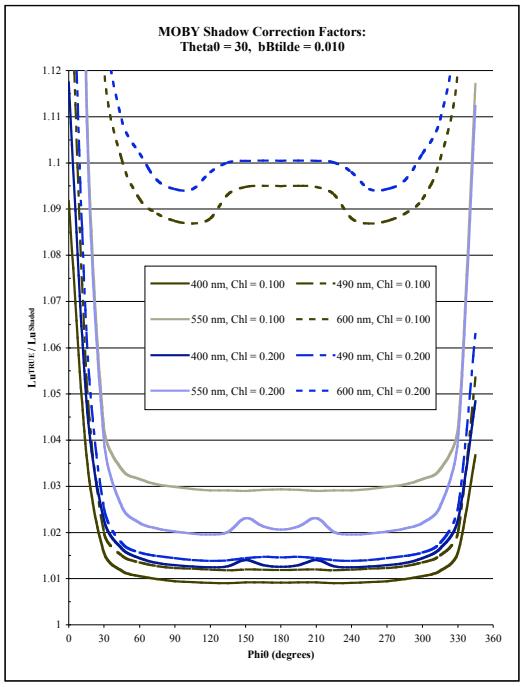

a.

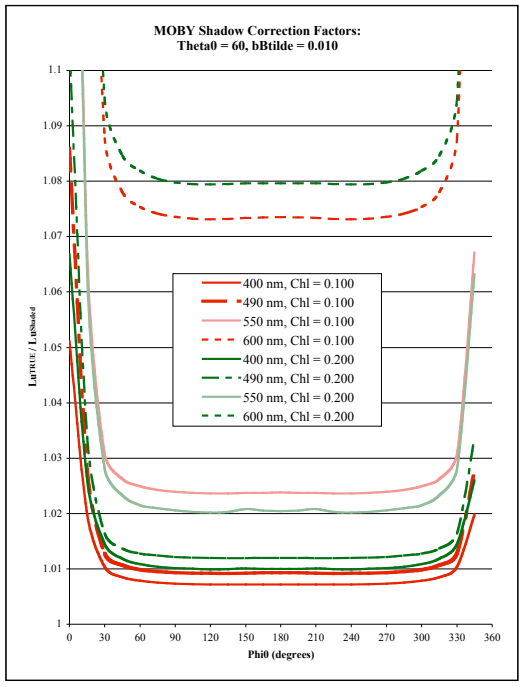

b.

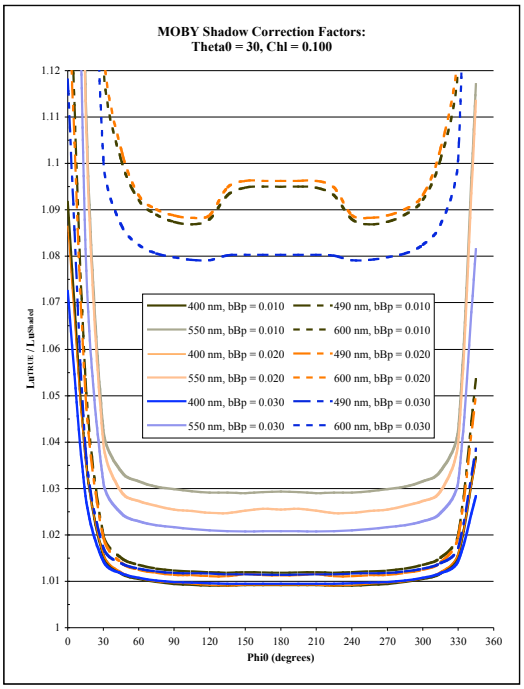

c.

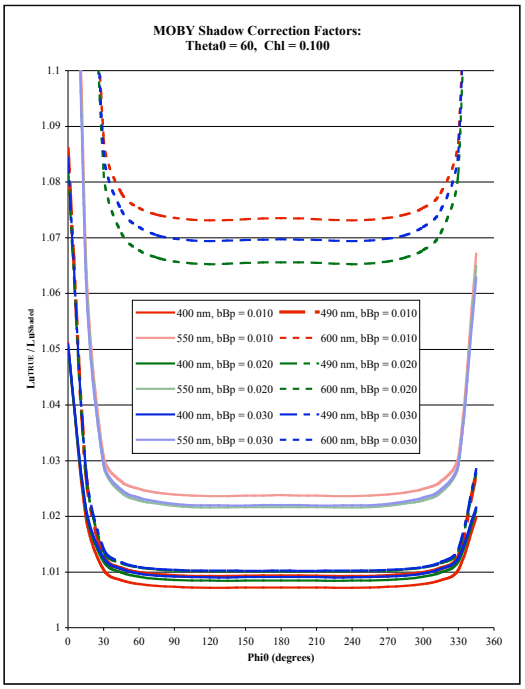

d.

Fig. 6.5: Variations of MOBY self-shading corrections over solar azimuth at solar zenith 30 deg (**a & c**) and 60 deg (**b & d**), comparing $\tilde{b}_{bp} = 0.010$ at 4 wavelengths and 2 "Chl" indices (**a & b**), and evolution for $\tilde{b}_{bp} = 0.01,\ 0.02$ & 0.03 at Chl = 0.100 (**c & d**).

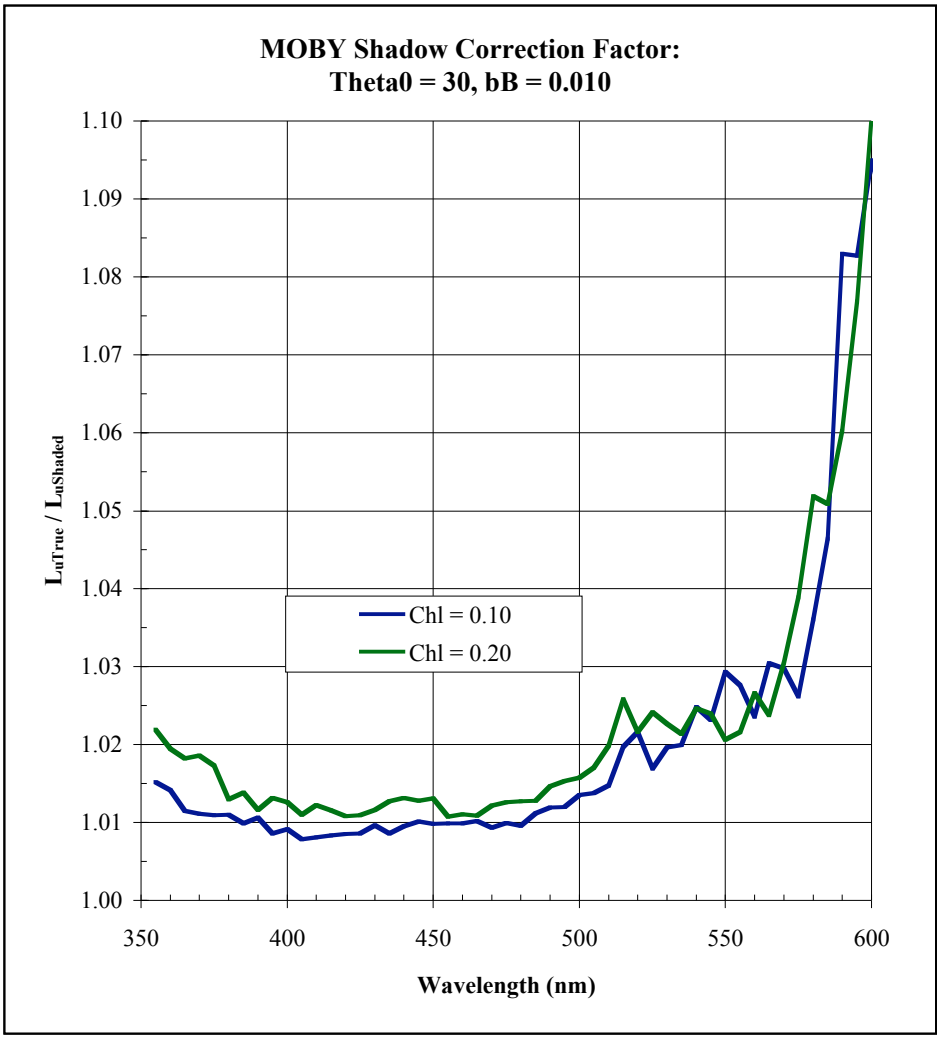

Fig. 6.6: Spectral distribution of MOBY Self-Shading Factors for $\tilde{b}_{bp} = 0.010$ & $(\theta_0, \phi_0) = (30°, 180°)$ and $Chl = 0.10$ (Blue) and 0.20 (Green). [Cf. Fig. 6.5a above] Increase in self-shading with increasing *Chl* is significantly apparent above the Monte Carlo noise level for wavelengths < 515 nm, but becomes lost in the increased noise of solutions as absorption by water increases rapidly with increasing wavelength beyond that.

Discussion and Recommendations

The MH1 results provide tables of MOBY instrument self-shading correction factors $R_{ISS}^{MOBY}\left(Z_{hms}, \lambda; Chl, \tilde{b}_{bp}, \theta_0, \phi_0\right)$ for 80 wavelengths at 4 depths, 6 solar zenith angles, 13 solar azimuth angles (invoking left right symmetry), 5 particle scattering phase functions, and 16 IOP Index *Chl* levels (which only qualitatively correspond to HPLC concentrations of chlorophyll) (Table 6.1, p17 above). Combining these data into a single 6-dimensional tensor floating-point array would occupy

approximately 8 Megabytes of memory, which is entirely feasible in most modern desktop computers. There are, however, other ways to organize the data and work with much smaller sub-arrays if memory is limited in a particular computer environment.

The underlying MH1 intermediate product files comprise a database that is about 4 Gigabytes in size, and it will be delivered on a DVD-R. The intermediate data products will be needed to tune the $R_{\mathrm{ISS}}^{\mathrm{MOBY}}\left(Z_{\mathrm{hms}},\lambda;Chl,\tilde{b}_{\mathrm{bp}},\theta_0,\phi_0\right)$ tables to validate and improve match-ups between MOBY measured upwelling radiance and appropriate MH1 IOP cases. We return to this topic below, at the end of this section.

The examination of the MH1 MOBY ISS factors, in the previous section, shows that:

1. $R_{\mathrm{ISS}}^{\mathrm{MOBY}}\left(Z_{\mathrm{hms}},\lambda;Chl,\tilde{b}_{\mathrm{bp}},\theta_0,\phi_0\right)$ when $\theta_0 > 20°$ and $|\phi_0| \gtrsim 45°$ is weakly sensitive to Z_{hms}, the depth of the horizontal monitoring surface containing each sensor, but becomes strongly apparent when $|\phi_0| < 45°$. The observed Z_{hms}-dependence is probably due primarily to differences in the MOBY Boom/Spar cross-section dimensions at each depth, rather than to variations in the radiance distribution over this shallow range of depths. At any rate, using the appropriate $R_{\mathrm{ISS}}^{\mathrm{MOBY}}\left(Z_{\mathrm{hms}},\lambda;Chl,\tilde{b}_{\mathrm{bp}},\theta_0,\phi_0\right)$ array for each depth is not burdensome.
2. $R_{\mathrm{ISS}}^{\mathrm{MOBY}}\left(Z_{\mathrm{hms}},\lambda;Chl,\tilde{b}_{\mathrm{bp}},\theta_0,\phi_0\right)$ is strongly sensitive to both solar zenith and azimuth angles.
    a. Ideally, the MOBY data should not be used for vicarious calibration of satellite sensors for $\theta_0 \le 20°$. Even were sun glint not excessive in this solar zenith range, the larger $R_{\mathrm{ISS}}^{\mathrm{MOBY}}$ values would introduce significant uncertainties as well.
    b. Likewise, $R_{\mathrm{ISS}}^{\mathrm{MOBY}}\left(Z_{\mathrm{hms}},\lambda;Chl,\tilde{b}_{\mathrm{bp}},\theta_0,\phi_0\right)$ increases rapidly as solar azimuth decreases into the range $|\phi_0| \lesssim 45°$ (Figs. 6,3, 6.4 and 6.5). Uncertainty of even a few degrees in determining ϕ_0 (especially if $\theta_0 \le 20°$), and errors in interpolation between ϕ_{B} sectors (Fig. 3.1, p9 above), will introduce unacceptably large and difficult to quantify uncertainty into the corrected upwelling radiances.
3. $R_{\mathrm{ISS}}^{\mathrm{MOBY}}\left(Z_{\mathrm{hms}},\lambda;Chl,\tilde{b}_{\mathrm{bp}},\theta_0,\phi_0\right)$ is significantly sensitive to both *Chl* and $\tilde{b}_{\mathrm{bp}}$, and in both cases the degree of sensitivity depends on λ and θ_0. For $\lambda \lesssim 515$ nm, when $\theta_0 \ge 30°$ $\Delta R_{\mathrm{ISS}}^{\mathrm{MOBY}} \sim 0.003$ per $\Delta Chl = 0.1$ (Figs. 6.4 and 6.5), when $\theta_0 = 20°$ $\Delta R_{\mathrm{ISS}}^{\mathrm{MOBY}} \sim 0.005$ per $\Delta Chl = 0.1$ and when $\theta_0 = 10°$ $\Delta R_{\mathrm{ISS}}^{\mathrm{MOBY}} \sim 0.007$ per $\Delta Chl = 0.1$. For $\lambda \lesssim 515$ nm and $\theta_0 \ge 30°$, $\Delta R_{\mathrm{ISS}}^{\mathrm{MOBY}} \sim 0.0025$ per $\Delta b_{\mathrm{bp}} = 0.01$ (Fig. 6.5) and we did not evaluate sensitivity to $\tilde{b}_{\mathrm{bp}}$ at lower zenith angles. At wavelengths $\lambda \gtrsim 550$ nm sensitivity to *Chl* and $\tilde{b}_{\mathrm{bp}}$ is masked by noise associated with increasing uncertainty in AMC RT solutions as absorption by water increases sharply.
4. At wavelengths $\lambda \lesssim 515$ nm the apparent noise fluctuations in MH1 $R_{\mathrm{ISS}}^{\mathrm{MOBY}}$ spectra are ~0.002 in magnitude, but as wavelength increases beyond that limit, the noise fluctuations increase to $\gtrsim 0.005$ at 550 nm and beyond. These fluctuations are a direct result of increasing uncertainty in a highly absorbing medium (water) in Adjoint Monte Carlo solutions tracing only 10^6 photon packets at each wavelength. Preliminary tests indicate that we can reduce these uncertainties by a factor of ~2 by increasing the number of photon packets traced by a factor of 4. However, in this wavelength region we would still be imposing very large

relative corrections on very small values of upwelling radiance, and further discussion is needed to clarify the motivation for, and cost effectiveness of, pursuing self-shading corrections in this wavelength domain.

In the original proposal that was supported under this NOAA grant, we ambitiously envisioned a comprehensive study of 2- and 3-dimensional self-shading effects for the MOBY case, and self-shading studies of oddly shaped radiometer housings in varied, turbid water masses. Available time and resources under this grant were insufficient to support the level-of-effort required to address all of these aspects of the general problem of self-shading in upwelling radiance measurements.

That said, the MH1 results reported here successfully address what is perhaps the most important question motivating this research: "What are the IOP and solar zenith and azimuth dependencies that govern self-shading of MOBY upwelling radiance measurements by its spar-buoy and sensor standoff booms?" These factors are the key to accurately correcting self-shading artifacts in exact normalized water-leaving radiance spectra determined from MOBY data for vicarious calibration of satellite ocean color sensors. The MH1 results also clearly identify ranges of solar azimuth (relative to the MOBY boom orientation) where self-shading corrections are too large and uncertain to support vicarious calibration.

It was necessary to address the MOBY upwelling radiance self-shading problem via the vertically homogeneous, modeled IOP assumptions that underlie the MH1 models, because there are no routinely measured IOP accompanying MOBY $L_{\mathrm{u}}\left(Z_{\mathrm{hms}},\lambda\right)$ measurements. If $L_{\mathrm{u}}\left(Z_{\mathrm{hms}},\lambda\right)$ measurements were made concurrently with IOP measurements sufficient to determine $a\left(Z_{\mathrm{hms}},\lambda\right), c\left(Z_{\mathrm{hms}},\lambda\right), \& \, b_{\mathrm{b}}\left(Z_{\mathrm{hms}},\lambda\right)$, it would be straightforward to apply the methods and software adapted, developed (AMC RT) and applied (HYDROLIGHT) in this study to calculate self-shading corrections directly. Supporting IOP measurements are a critical prerequisite for self-shading corrections in any water mass conditions more turbid, or vertically varied, than the stable clear-water environment typical of the MOBY site off Lanai, Hawaii. On the other hand, if sufficient IOP measurements are available, it is not difficult to apply the methods and software used here to calculate 2-D self-shading corrections for oddly shaped platform/instrument configurations. [Additional research and development would be necessary to incorporate 3-D effects, although these effects could be addressed on a case-by-case basis using the more traditional method of matching backward AMC RT photon-packet trajectories to a specified incident radiance distribution above the sea surface.]

The unfinished aspect of the MH1 self-shading model and algorithm is to develop and validate a robust method for matching self-shaded measured MOBY upwelling radiance spectra $L_{\mathrm{uS}}^{\mathrm{MOBY}}\left(Z,\lambda,\theta_0,\phi_0\right)$ to IOP conditions, as parameterized by the *Chl* IOP-Index. This amounts to finding a *Chl* case where the spectral characteristics of $L_{\mathrm{u}}\left(Z,\lambda;Chl,\tilde{b}_{\mathrm{bp}},\theta_0\right)$ (computed with HYDROLIGHT using MH1 IOP models) match those of $R_{\mathrm{ISS}}^{\mathrm{MOBY}}\left(Z_{\mathrm{hms}},\lambda;Chl,\tilde{b}_{\mathrm{bp}},\theta_0,\phi_0\right)$-corrected $L_{\mathrm{u}}^{\mathrm{MOBY}}\left(Z,\lambda,\theta_0,\phi_0\right)$ measurements. We close by briefly outlining and discussing some key elements of a possible approach to an MH1 IOP Selection method:

1. The method must take account of variations in $L_{\mathrm{u}}^{\mathrm{MOBY}}\left(Z,\lambda;Chl,\tilde{b}_{\mathrm{bp}},\theta_0,\phi_0\right)$ relative to otherwise matching MH1 $L_{\mathrm{u}}\left(Z,\lambda;Chl,\tilde{b}_{\mathrm{bp}},\theta_0\right)$, due to differences between MH1 and actual $L_{\mathrm{d}}\left(0_{\mathrm{air}},\lambda,\theta_0,\phi_0\right)$ spectral radiance distributions incident on the sea surface. The use of relative ISS corrections, together with scaling by ratios of actual and MH1 downwelling irradiance, will also reduce sensitivity to this effect.
2. The analytic equations (6.1) and (6.2) [p16 above] that are used to determine $a_{\mathrm{p}}\left(\lambda;Chl\right)$ and $b_{\mathrm{p}}\left(\lambda;Chl\right)$, yield AMC RT and HYDROLIGHT $L_{\mathrm{u}}\left(Z,\lambda;Chl,\tilde{b}_{\mathrm{bp}},\theta_0\right)$ spectra that can be systematically inverted to estimate *Chl*. For example, Fig. 6.7a shows the least-squares fit to a cubic Hermitian Finite Element (HFE) function giving estimates of $Chl\left[\dfrac{L_{\mathrm{u}}\left(1.3,440;Chl,0.015,0\right)}{L_{\mathrm{u}}\left(1.3,550;Chl,0.015,0\right)}\right]$, and Fig. 6.7b shows the fit to a similar HFE model of estimates $Chl\left[\bar{K}_{L_{\mathrm{u}}}\left(1.3,5.1;440\right)\right]$, both for a zenith sun, the depth(s) of MOBY radiance measurements, and $\tilde{b}_{\mathrm{bp}}=0.015$.
3. Inelastic scattering contributions are a significant part of self-shaded MOBY measurements $L_{\mathrm{uS}}^{\mathrm{MOBY}}\left(Z,\lambda;Chl,\tilde{b}_{\mathrm{bp}},\theta_0,\phi_0\right)$. In contrast, the AMC RT and HYDROLIGHT computations of $L_{\mathrm{u}}\left(Z,\lambda;Chl,\tilde{b}_{\mathrm{bp}},\theta_0\right)$ include only elastic scattering processes. If we assume that CDOM fluorescence is negligible in the MOBY site, and that chlorophyll *a* fluorescence is also negligible at wavelengths $\lambda \lesssim 650$ nm, we need to consider only Raman Scattering contributions. This is most easily accomplished by running a second series of HYDROLIGHT computations, for each combination of *Chl*, $\tilde{b}_{\mathrm{bp}}\left(\lambda\right)$, and θ_0, with Raman scattering turned on to calculate $L_{\mathrm{u}}^{\mathrm{Raman}}\left(Z,\lambda;Chl,\tilde{b}_{\mathrm{bp}},\theta_0\right)$, which includes effects of both elastic and Raman scattering (Mobley 1994; Mobley and Sundman 2000a, 2000b). In Fig. 6.8 are compared, for example, curves of $L_{\mathrm{u}}\left(1.3,\lambda;Chl,0.015,0\right)$ and $L_{\mathrm{u}}^{\mathrm{Raman}}\left(1.3,\lambda;Chl,0.015,0\right)$ for $Chl=0.05,0.1,0.2,\&\ 0.3$; water-Raman scattering contributions are small but significant. It is convenient to define a relative Raman factor

$$\delta_{L_{\mathrm{u}}}^{\text{Water-Raman}}\left(Z,\lambda;Chl,\tilde{b}_{\mathrm{bp}},\theta_0\right)\equiv\frac{L_{\mathrm{u}}^{\mathrm{Raman}}\left(Z,\lambda;Chl,\tilde{b}_{\mathrm{bp}},\theta_0\right)}{L_{\mathrm{u}}\left(Z,\lambda;Chl,\tilde{b}_{\mathrm{bp}},\theta_0\right)}-1, \qquad (6.5)$$

so that we can express unshaded radiance, with Raman included as

$$L_{\mathrm{u}}^{\mathrm{Raman}}\left(Z,\lambda;Chl,\tilde{b}_{\mathrm{bp}},\theta_0\right)=L_{\mathrm{u}}\left(Z,\lambda;Chl,\tilde{b}_{\mathrm{bp}},\theta_0\right)\left[1+\delta_{L_{\mathrm{u}}}^{\text{Water-Raman}}\left(Z,\lambda;Chl,\tilde{b}_{\mathrm{bp}},\theta_0\right)\right]. \qquad (6.6)$$

Relative water-Raman factors $\delta_{L_{\mathrm{u}}}^{\text{Water-Raman}}\left(Z,\lambda;Chl,\tilde{b}_{\mathrm{bp}},\theta_0\right)$ corresponding to the spectra illustrated in Fig. 6.8, which are all unshaded radiance, are shown in Fig. 6.9a. We now assume that the instrument self-shading effects on Raman scattering at wavelength λ may be accounted for using the elastic scattering factors $R_{\mathrm{ISS}}^{\mathrm{MOBY}}\left(Z,\lambda_{\mathrm{EX}}^{\text{Water-Raman}};Chl,\tilde{b}_{\mathrm{bp}},\theta_0,\phi_0\right)$ for the water-Raman excitation wavelength $\lambda_{\mathrm{EX}}^{\text{Water-Raman}}$. Within the 5 nm wavelength resolution of the MH1 spectral $R_{\mathrm{ISS}}^{\mathrm{MOBY}}$ factors, it is sufficient to estimate a constant water-Raman wavenumber shift of –3400 cm^{-1} (Mobley 1994; pp292ff), and determine the excitation wavelength (within ~ 1 nm) as

$$\lambda_{\mathrm{EX}}^{\text{Water-Raman}} = \frac{10^7}{\frac{10^7}{\lambda} + 3400} \text{ nm}. \tag{6.4}$$

To obtain a modeled upwelling radiance counterpart to MOBY measurements, we write

$$L_{\mathrm{uS}}^{\text{Raman}}\left(Z,\lambda;Chl,\tilde{b}_{\mathrm{bp}},\theta_0\right) = L_{\mathrm{u}}\left(Z,\lambda;Chl,\tilde{b}_{\mathrm{bp}},\theta_0\right)\times \left[\frac{1}{R_{\mathrm{ISS}}^{\text{MOBY}}\left(Z,\lambda;Chl,\tilde{b}_{\mathrm{bp}},\theta_0,\phi_0\right)} + \frac{\delta_{L_{\mathrm{u}}}^{\text{Water-Raman}}\left(Z,\lambda;Chl,\tilde{b}_{\mathrm{bp}},\theta_0\right)}{R_{\mathrm{ISS}}^{\text{MOBY}}\left(Z,\lambda_{\mathrm{EX}}^{\text{Water-Raman}};Chl,\tilde{b}_{\mathrm{bp}},\theta_0,\phi_0\right)}\right]. \tag{6.7}$$

Estimates of self-shaded, relative water-Raman contributions (the send term in square brackets) are compared in Fig. 6.9b to the unshaded versions from 6.9a.

Finally, we may substitute the self-shaded MOBY upwelling radiance measurements in (6.7) to estimate the ISS corrected MOBY upwelling radiance, with Raman scattering removed, as

$$L_{\mathrm{u}}^{\text{MOBY}}\left(Z,\lambda;Chl,\tilde{b}_{\mathrm{bp}},\theta_0\right) = \frac{L_{\mathrm{uS}}^{\text{MOBY}}\left(Z,\lambda;Chl,\tilde{b}_{\mathrm{bp}},\theta_0\right)}{\frac{1}{R_{\mathrm{ISS}}^{\text{MOBY}}\left(Z,\lambda;Chl,\tilde{b}_{\mathrm{bp}},\theta_0,\phi_0\right)} + \frac{\delta_{L_{\mathrm{u}}}^{\text{Water-Raman}}\left(Z,\lambda;Chl,\tilde{b}_{\mathrm{bp}},\theta_0\right)}{R_{\mathrm{ISS}}^{\text{MOBY}}\left(Z,\lambda_{\mathrm{EX}}^{\text{Water-Raman}};Chl,\tilde{b}_{\mathrm{bp}},\theta_0,\phi_0\right)}}. \tag{6.8}$$

4. We envision an iterative procedure initialized by assuming a "typical" value of the particle backscattering fraction (here we have arbitrarily guessed at $\tilde{b}_{\mathrm{bp}} = 0.015$). We also need a first-guess value of *Chl*. Although HPLC determined chlorophyll concentration is not equivalent to *Chl*, its magnitude is similar, and it seems reasonable to assume a first guess value for *Chl* ~ 0.07, which is close to the peak of the MOBY chlorophyll concentration. These starting guesses, together with solar zenith and azimuth angles at the time of the MOBY measurement, provide enough information to calculate an initial guess at $L_{\mathrm{u}}^{\text{MOBY}}\left(Z,\lambda;Chl,\tilde{b}_{\mathrm{bp}},\theta_0\right)$ with equation (6.8). We might then adapt the approach of Morel and Gentili (1996) to determine a "normalized" upwelling radiance at each Z_{hms} as

$$L_{\mathrm{u}}^{\text{MOBY}}\left(Z_{\mathrm{hms}},\lambda;Chl,\tilde{b}_{\mathrm{bp}},0\right) = L_{\mathrm{u}}^{\text{MOBY}}\left(Z_{\mathrm{hms}},\lambda;Chl,\tilde{b}_{\mathrm{bp}},\theta_0\right)\frac{E_{\mathrm{d}}\left(Z_{\mathrm{hms}},\lambda;Chl,\tilde{b}_{\mathrm{bp}},0\right)}{E_{\mathrm{d}}\left(Z_{\mathrm{hms}},\lambda;Chl,\tilde{b}_{\mathrm{bp}},\theta_0\right)}\times \frac{f_0\left(Z_{\mathrm{hms}},\lambda;Chl,\tilde{b}_{\mathrm{bp}},0\right)}{f_n\left(Z_{\mathrm{hms}},\lambda;Chl,\tilde{b}_{\mathrm{bp}},\theta_0\right)}\frac{Q_n\left(Z_{\mathrm{hms}},\lambda;Chl,\tilde{b}_{\mathrm{bp}},\theta_0\right)}{Q_0\left(Z_{\mathrm{hms}},\lambda;Chl,\tilde{b}_{\mathrm{bp}},0\right)}. \tag{6.9}$$

The requisite data to determine ratios of downwelling irradiance, f – and Q-functions have been extracted from the MH1 series of HYDROLIGHT output and are included in the MH1 reciprocity solution output files. We could then use values from this first-guess $L_{\mathrm{u}}^{\text{MOBY}}\left(Z,\lambda;Chl,\tilde{b}_{\mathrm{bp}},0\right)$ spectrum to compute a second iteration *Chl* estimate from either of the relationships illustrated in Figs. 6.7a or 6.7b (or something similar in concept), and proceed until convergence is obtained.

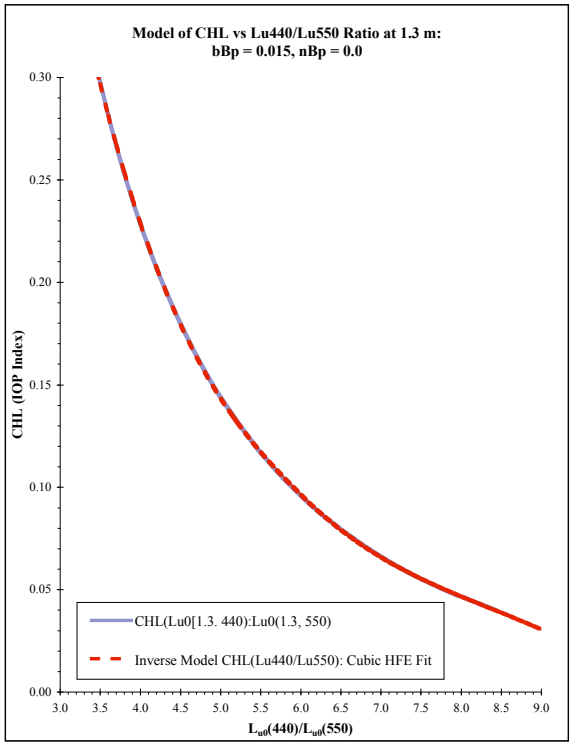

a.

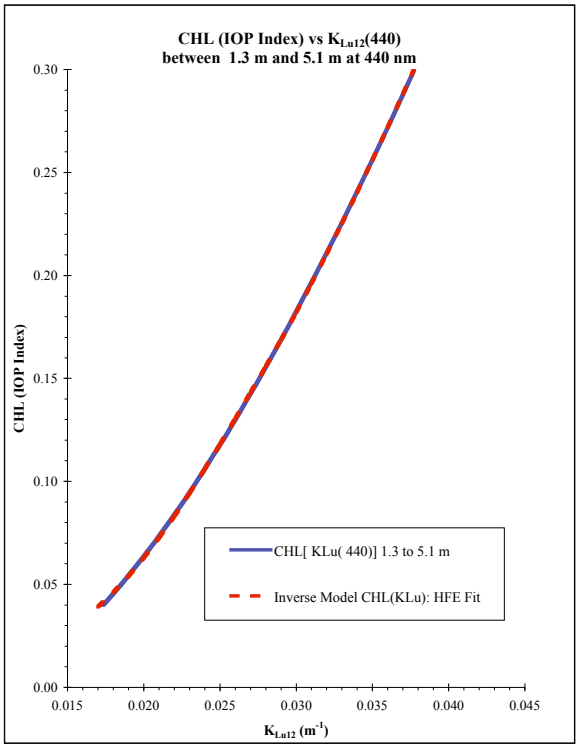

b.

Fig. 6.7: Inverse models (Cubic HFE Least Squares Fits) giving the IOP Index *Chl* as a function of the ratio of upwelling radiances at 440 and 550 nm, $\frac{L_u(1.3,440)}{L_u(1.3,550)}$ at a depth of 1.3 m (**a**), and as a function of the diffuse attenuation coefficient for upwelling radiance at 440 nm $K_{L_u}^{12}(440)$ between the depths of the first (1.3 m) and second (5.1 m) MOBY radiance sensors (**b**).

The application of MH1 ISS corrections to MOBY upwelling radiance spectra is greatly simplified if we restrict the problem to MBOY measurements at $\lambda \lesssim 600$, $\theta_0 \gtrsim 25°$ and $|\phi_0| > 60°$. Under these constraints, were we to assume that a 2(Standard Uncertainty) of $\tilde{b}_{bp}$ at the MOBY site is $0.010 \le \tilde{b}_{bp} \le 0.020$ and set $\tilde{b}_{bp} = 0.015$, the resulting 1 Std. Uncertainty contribution to the uncertainty budget of R_{ISS}^{MOBY} would be ~0.0012, which would not significantly alter the estimate AMC contributed uncertainty of ~0.002 for $\lambda < 515$ nm and would have no impact whatever on the >0.005 uncertainty at longer wavelengths. If we also assume the Standard Uncertainty is 0.050 for *Chl* IOP-Index estimates from $L_u^{MOBY}(Z,\lambda;Chl,\tilde{b}_{bp},0)$ using either, or a combination, of the wavelength ratio or K_{Lu} algorithms illustrated in Fig. 6.7, the resulting ~0.0015 uncertainty contribution to R_{ISS}^{MOBY} is similarly negligible. That level of *Chl* uncertainty is probably grossly conservative. Although HPLC chlorophyll *a* concentration data cannot be substituted for radiometrically determined *Chl* in this context, the magnitudes of regional averages and space-time variance of the two variables may be expected to closely track each other. A histogram of the multi-year record of HPLC chlorophyll measurements at the MOBY site (Pers. Comm.: S. Flora, SJSU MLML, Moss Landing CA) strongly resembles a log-normal distribution, with a maximum (mode) frequency of 0.07 mg m^{-3}, and a

visually estimated half-width ~0.03 mg m^{-3}. One could find the actual mode, mean and variance of a log-normal distribution fitted to these data, but clearly the 0.05 uncertainty

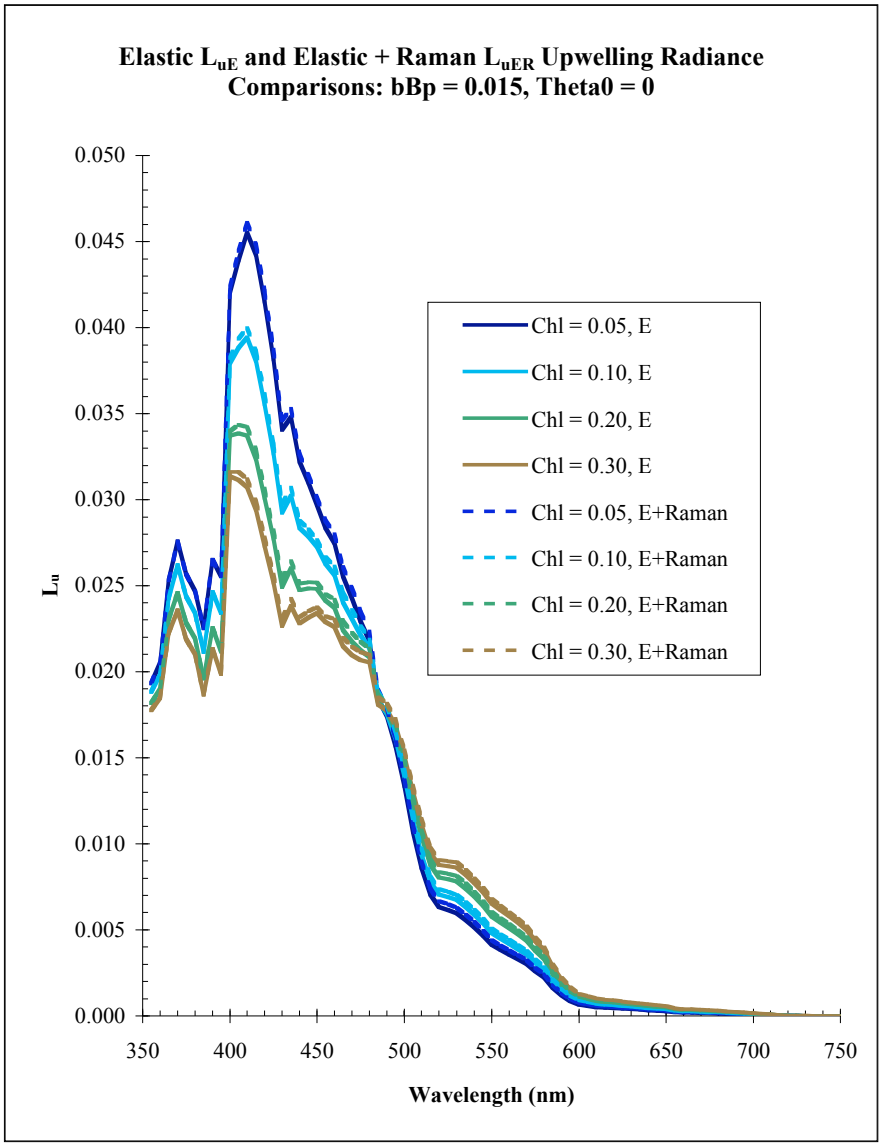

Fig. 6.8: Comparisons of Hydrolight upwelling radiance spectra $L_u(1.3,\lambda;Chl,0.015,0,\bullet)$ for elastic scattering only without Raman scattering (solid curves), and with Raman Scattering $L_u^{\text{Raman}}(1.3,\lambda;Chl,0.015,0,\bullet)$, *i.e.* for $Z_{\text{hms}} = 1.3$ m, $\tilde{b}_{\text{bp}} = 0.015$, $\theta_0 = 0°$ and $\phi_0 \Rightarrow \bullet$ is indeterminate.

guess for *Chl* would be consistent with the 1 Std Uncertainty of the environmental variation of chlorophyll concentration, without trying to refine it for an individual observation using, *e.g.* a ratio algorithm. We can safely expect the uncertainty of iterative *Chl* estimates to have a much smaller standard uncertainty, once an appropriate analysis is completed.

Additional research will be needed to develop and validate a method for applying the MH1 (or a future modification) $R_{\text{ISS}}^{\text{MOBY}}$ correction factors to MOBY upwelling radiance measurements. There is reason to be optimistic that an iterative scheme along the lines outlined above will lead to a robust method. Nevertheless, the analyses must be done to first verify that the method will converge, and to then determine estimates of the uncertainty of the resulting corrections.

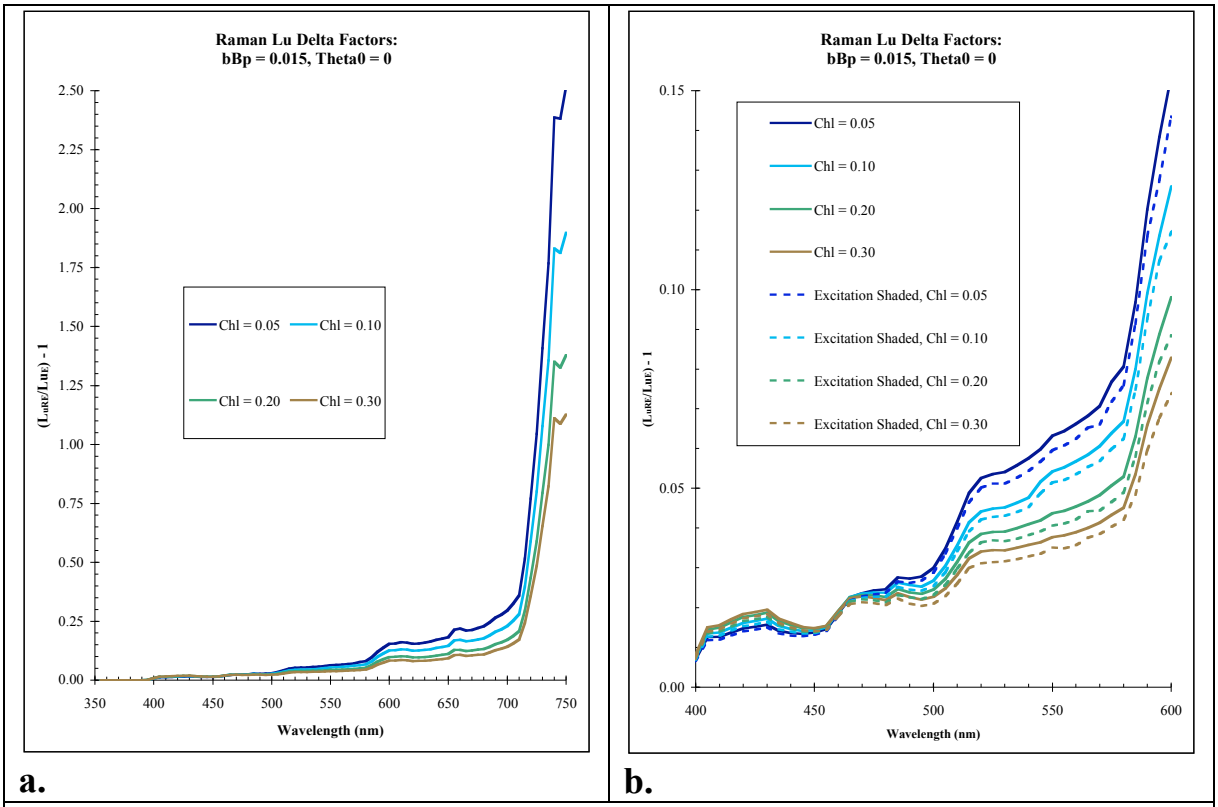

Fig. 6.9: **a**) Raman scattering relative contributions to upwelling radiance $\delta_{L_u}^{\text{Raman}}(1.3,\lambda;Chl,0.015,0,\bullet)=\dfrac{L_u^{\text{Raman}}(1.3,\lambda;Chl,0.015,0,\bullet)}{L_u(1.3,\lambda;Chl,0.015,0,\bullet)}-1$ for nadir viewing radiance at $Z_{\text{hms}}=1.3$ m, $\tilde{b}_{\text{bp}}=0.015$, $\theta_0=0°$ and $\phi_0\Rightarrow\bullet$ is indeterminate. **b**) Same as (**a**) showing $\delta_{L_u}^{\text{Raman}}(1.3,\lambda;Chl,0.015,0,\bullet)$ [solid curves] on an expanded scale in the wavelength range $400\le\lambda\le600$ nm, and comparing the effect of instrument self shading at the water Raman excitation wavelengths $\dfrac{\delta_{L_u}^{\text{Raman}}(1.3,\lambda;Chl,0.015,0,\bullet)}{R_{\text{ISS}}^{\text{MOBY}}(1.3,\lambda_{\text{EX}};Chl,0.015,0,\bullet)}$ [dashed curves].

References

Case, K.M., 1957: Transfer problems and the reciprocity principle. *Rev Modern Phys*., **29**(4): 651-663.

Clark, D.K., and OTHERS, 2003 MOBY, a radiometric buoy for performance monitoring and vicarious calibration of satellite ocean color sensors: measurement and data analysis protocols. Chapter 2 in: Mueller *et al*., 2003. *Ocean Optics Protocols for Satellite Ocean Color Sensors, Revision 4, Volume VI: Special Topics in Ocean Optics Protocols, and Appendices*. J.L. Mueller, G.S. Fargion and C.R. McClain [Eds.], NASA/TM-2003-211621/Rev4-VolVI, NASA GSFC, Greenbelt, MD, pp3-34.

Fournier, G. and J.L Forand, 1994: Analytic phase function for ocean water, in *Ocean Optics XII,* J.S. Jaffe [Ed.], Proc. SPIE **2258**: 194-201.

Gordon, H. R., 1985. Ship perturbation of irradiance measurements at sea. l: Monte Carlo simulations. *Appl. Opt.* **24**(23): 4172-4182.

Gordon, H.R. and D.K. Clark, 1981. Clear water radiances for atmospheric correction of coastal zone color scanner imagery. *Appl. Opt*., 20(24): 4175-4180.

Gordon, H.R. and K. Ding, 1992. Self-shading of in-water optical instruments. *Limnol. Oceanogr*., **37**(3): 491-500.

Gordon, H.R. and A. Morel, 1983: *Remote Assessment of Ocean Color for Interpretation of Satellite Visible Imagery, A Review; Lecture Notes on Coastal and Estuarine Studies, Vol. 4*, Springer-Verlag, New York, 114pp.

Kou, L., D. Labrie and P. Chylek, 1993: Refractive indices of water and ice in the 0.65 to 2.5 μm spectral range, *Appl. Opt.*, **32:** 3531-3540.

Kuwajara. V.S. and OTHERS, 2003: Radiometric and bio-optical measurements from moored and drifting buoys: measurement and data analysis protocols. Chapter 3 in: Mueller *et al*., 2003. *Ocean Optics Protocols for Satellite Ocean Color Sensors, Revision 4, Volume VI: Special Topics in Ocean Optics Protocols, and Appendices*. J.L. Mueller, G.S. Fargion and C.R. McClain [Eds.], NASA/TM-2003-211621/Rev4-VolVI, NASA GSFC, Greenbelt, MD, pp35-78.

Mobley, C.D. 1994. *Light and Water: Radiative Transfer in Natural Waters*, Academic Press, San Diego, 592pp.

Mobley, C.D. and L.K. Sundman, 2000a: *HYDROLIGHT 4.1 User's Guide*, Sequoia Scientific, Inc., Redmond, WA, 86pp

Mobley, C.D. and L.K. Sundman, 2000b: *HYDROLIGHT 4.1 Technical Documentation*, Sequoia Scientific, Inc., Redmond, WA, 76pp

Morel, A., 1974: Optical properties of pure water and pure sea water. In: *Optical Aspects of Oceanography*, N.G. Jerlov and E.S. Nielson, Eds., pp1-23.

Morel, A. and B. Gentilli, 1996. Diffuse reflectance of oceanic waters. III. Implication of bidirectionality for the remote-sensing problem. *Appl. Opt.*, 35(24): 4850-4862.

Morel A. and S. Maritorena, 2000: Bio-optical properties of oceanic waters: a reappraisal. *J. Geophys. Res.*, **106:** 7163-7180.

Pope, R.M. and E.S. Fry. 1997: Absorption spectrum (380-700 nm) of pure water. II. Integrating cavity measurements. *Appl. Opt*. **36**: 8710-8723.

Prieur, L. and S. Sathyendranath, 1981. An optical classification of coastal and oceanic waters based on the specific spectral absorption curves of phytoplankton pigments, dissolved organic matter, and other particulate materials. *Limnol. Oceanogr*. **26(4):** 671-689.

Smith, R.C. and K.S. Baker, 1981. Optical properties of the clearest natural waters (200-800 nm). *Appl Opt.* **20** (2). 177-184.

Sogandares, F.M. and E.S. Fry, 1997. Absorption spectrum (340-640 nm) of pure water. I. Photothermal measurements. *Appl. Opt.*, **36(33):** 8699-8709.